LAWRENCE
LIVERMORE
NATIONAL
LABORATORY

LLNL-TR-607997

FY12 LLNL OMEGA Experimental Programs

R. Heeter, K. Fournier, K. Baker, P. Celliers, D. Fratanduono, J. Hawreliak, R. Kirkwood, A. Kritcher, A. Lazicki, T. Ma, B. Maddox, A. Pak, H. S. Park, R. Patterson, F. Perez, Y. Ping, C. Plechaty, J. Ross, R. Rygg, V. Smalyuk, R. Tommasini, C. Wehrenberg, G. W. Collins, W. Hsing, O. Landen

December 13, 2012

Disclaimer

This document was prepared as an account of work sponsored by an agency of the United States government. Neither the United States government nor Lawrence Livermore National Security, LLC, nor any of their employees makes any warranty, expressed or implied, or assumes any legal liability or responsibility for the accuracy, completeness, or usefulness of any information, apparatus, product, or process disclosed, or represents that its use would not infringe privately owned rights. Reference herein to any specific commercial product, process, or service by trade name, trademark, manufacturer, or otherwise does not necessarily constitute or imply its endorsement, recommendation, or favoring by the United States government or Lawrence Livermore National Security, LLC. The views and opinions of authors expressed herein do not necessarily state or reflect those of the United States government or Lawrence Livermore National Security, LLC, and shall not be used for advertising or product endorsement purposes.

This work performed under the auspices of the U.S. Department of Energy by Lawrence Livermore National Laboratory under Contract DE-AC52-07NA27344.

FY12 LLNL OMEGA Experimental Programs

R. HEETER, K. FOURNIER, K. BAKER, P. CELLIERS, D. FRATANDUONO, J. HAWRELIAK, R. KIRKWOOD, A. KRITCHER, A. LAZICKI, T. MA, B. MADDOX, A. PAK, H.-S. PARK, R. PATTERSON, F. PEREZ, Y. PING, C. PLECHATY, J. ROSS, R. RYGG, V. SMALYUK, R. TOMMASINI, C. WEHRENBERG, G. W. COLLINS, W. HSING, O. LANDEN

In FY12, LLNL conducted several campaigns on the OMEGA laser system and on the EP laser system, as well as campaigns that used the OMEGA and EP beams jointly. Overall LLNL led 325 target shots involving the OMEGA laser system and 121 target shots involving the EP laser system. Approximately 38% of the total number of shots (129 OMEGA shots, 39 EP shots) shots supported the National Ignition Campaign (NIC). The remaining 197 OMEGA shots and 82 EP shots were dedicated to experiments for High-Energy-Density Physics (HED).

This work performed under the auspices of the U.S. Department of Energy by Lawrence Livermore National Laboratory under Contract DE-AC52-07NA27344.

Table of Contents:

NATIONAL IGNITION CAMPAIGN EXPERIMENTS 3
Thermal Conductivity Study of CH/Be and CH/D2 interfaces by refraction-enhanced x-ray radiography (AtwoodNum - PI: Y. Ping) 3
High-resolution measurements of velocity nonuniformities created by microscopic perturbations in NIF ablator materials (CAPSEED - PI: P. Celliers and M. Barrios) 4
Measuring the adiabatic index of polystyrene using counter-propagating shocks and x-ray Thomson scattering (HeatCap - PI: A. Pak) 6
Ablator Opacity Measurements (AblatOp - PI: R. Heeter) 9
Multi-Pump Stimulated Raman Scattering (SRSMultiPump - PI: R. Kirkwood) 12
Comparison of Plastic and High-Density Carbon Ablator Performance (HDCEnerg - PI: S. Ross) 13
Shock Release of ICF Relevant Materials (CHD2Rel - PI: D. Fratanduono) 14

HIGH-ENERGY-DENSITY EXPERIMENTS 15

I. Material Dynamics and Equation-of-state 15
Tantalum Rayleigh-Taylor Experiments (ICETaRT, PI H.-S. Park) 15
Iron Rayleigh-Taylor Experiments (ICE-Iron-RT, PI C. Plechaty) 15
Double Pulse Radiography Development (DblPulse PI C. Plechaty) 19
Diffraction Studies on Shocked Tantalum (StrDiff, TaRDiff, ShkLaue and EP-TaBragg; - PIs: B. Maddox, A. Comley and C. Wehrenberg) 22
Tantalum X-Ray Diffraction with Ramp Compression (TaXrayDiff, PI A. Lazicki) 24
Hydrogen Equation of State (H2EOS, PI A. Lazicki) 25
XAFS Study of Ramp-Compressed Fe, Ta and Mo (XAFS PI Y. Ping) 26
Tin Melt (TinMelt-12, PI A. Lazicki) 27
Gigabar Equation of State (GbarEOS-12, PI J. Hawreliak) 28
Equation of state for Foams Using Omega-EP (EP-Foam-12, PI J. Hawreliak) 27
Advanced X-Ray Diffraction Techniques (AdvXRD, PI J. Hawreliak) 30

II. Radiation Transport
Heated Wall Radiation Transport (HeatedWall, PI: K. Baker) 31
Fused Silica VISAR Window Test (Crystal Window, PI: B. Maddox) 32

III. High-Temperature Plasma Opacity 31
High-Temperature Plasma Opacity Experiments on Omega and Omega-EP (PI: R.F. Heeter with S. Chen, G.V. Brown and R.E. Marrs) 33

IV. Burn Physics 34
Non-LTE Transport and Nuclear Lifetimes (PI: A. Kritcher) 33

V. Hydrodynamics 34
Short-pulse, UV backlighting development for NIF (TinMan-12, PI: Vladimir Smalyuk) 36

VI. X-Ray Source Development and Applications 38
X-Ray Source Development with Nanostructured Materials (NanoStructure-12, PI R. Patterson) 38
Solar Cell Electrostatic Discharge (SolarCellESD-12, PI R. Patterson) 39

National Ignition Campaign Experiments

Thermal conductivity study of CH/Be and CH/D2 interfaces by refraction-enhanced x-ray radiography (AtwoodNum - PI: Y. Ping)

Y. Ping, O. L. Landen, J. A. Koch, R. Wallace, G. W. Collins

The Atwood#12A&B campaigns are based on the technique of time-resolved refraction-enhanced x-ray radiography that was successfully demonstrated in FY11. The evolution of the density profile at a cylindrical CH/Be interface isochorically heated by Ag L-band radiation has been measured in order to infer the thermal conductivity under ICF-relevant conditions. In addition to observation of the density evolution caused by thermal conduction, counter-propagating shock wave and rarefaction wave were also observed as shown in the Figure. The velocities of these waves were measured simultaneously, providing constraints on the temperature after heating. Preliminary analysis of the data and hydrodynamic simulations show that the thermal conductivity is higher than most models predict. The measurements of CH/D2 interface in cryogenic targets were complicated by leaking in the cryo cells, limited rotation movement and condensation on the backlighter which reduced the brightness significantly. A list of potential improvements has been provided to LLE for future experiments with cryogenic targets.

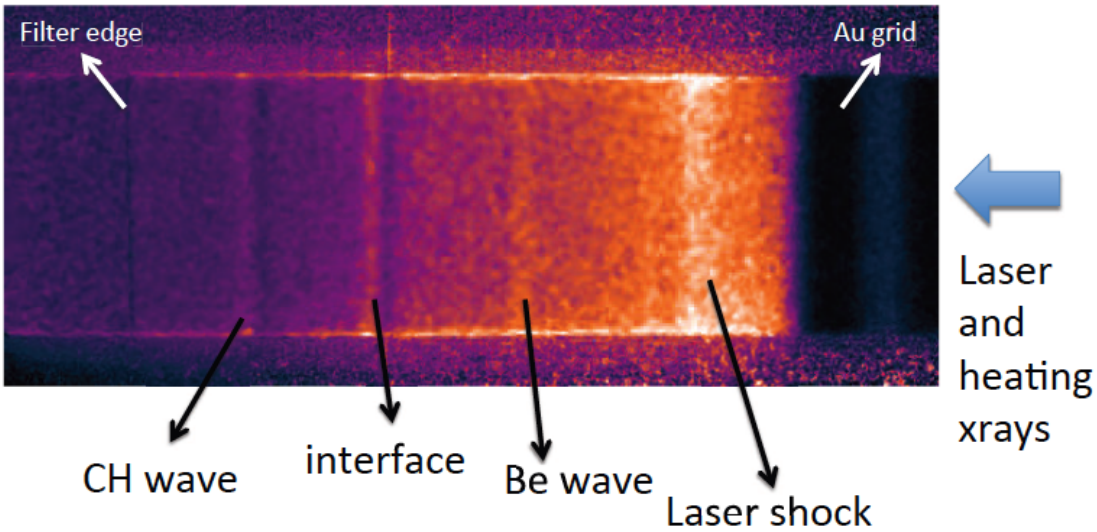

Figure 1: A radiograph of the heated CH/Be target. The delay between the heater and the backlighter was 5ns. The laser beams and heating x-rays were incident from the right side. Three fringes show up in the image, the middle one representing the interface, and two side ones corresponding to the waves propagating in CH and Be, respectively. The shock driven by the laser, traveling from right to left, is also visible.

High-resolution measurements of velocity nonuniformities created by microscopic perturbations in NIF ablator materials (CAPSEED – PI: P. Celliers with M.A. Barrios)

A full day of CAPSEED campaign took place in May 2012. This campaign is a continuation of earlier campaigns studying the performance of NIF ablators. The latest capsule designs using glow-discharge polymer (GDP) ablators for the National Ignition Campaign currently employed Si doping layers as preheat shielding for the fuel; the earlier NIC designs employed Ge doping layers. In response to this design change most of the CAPSEED-12A campaign was devoted towards assessing the performance of the newer Si-doped design (as compared to the previous Ge-doped designs). Results from this campaign (Fig. 1 below) show that the performance of the Si-doped material matches that of the Ge-doped material.

A further three shots were devoted towards studying double-shocked nano-crystalline diamond (or "high-density carbon", HDC). In current capsule designs employing diamond ablators the initial shock strength is only enough to melt the capsule partially. Shock strengths much higher than this will set the fuel adiabat higher than the design goal of current designs. Velocity fluctuations on the first (leading) shock are known to diminish significantly when the shock-melting starts. The purpose of the double-shock test is to see whether the second and third shocks that follow in the compression sequence accumulate further velocity fluctuations owing to the mixed-phase state of the diamond ablator following passage of the first shock. An initial double-shock test performed during the CAPSEED-12A campaign suggests (Fig. 2) that subsequent shocks appear to have similar fluctuation levels as the initial shock. Further tests are needed to extend the data set.

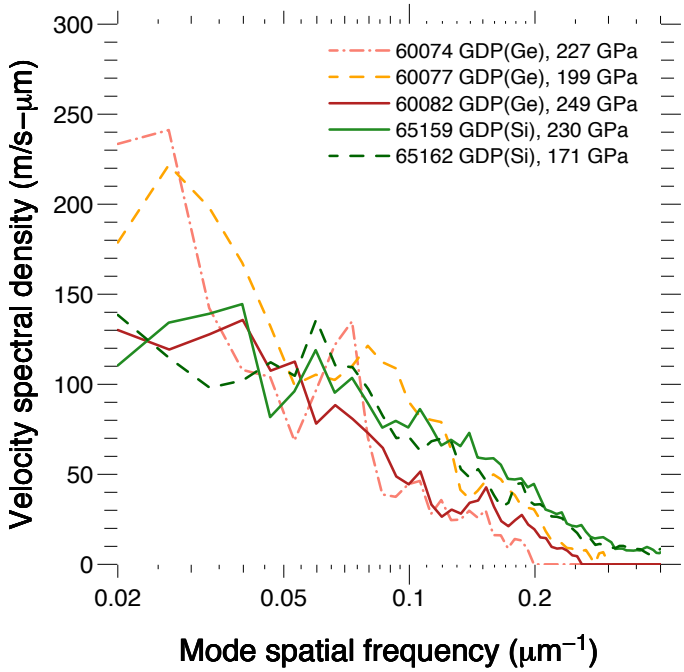

Figure 1: Velocity fluctuation spectra measured from for Ge-doped GDP in 2011 (60074, 60077 and 60082) and for Si-doped GDP in 2012 (65159 and 65162). The velocity spectra for all cases appear to be equivalent within the range of statistical fluctuations.

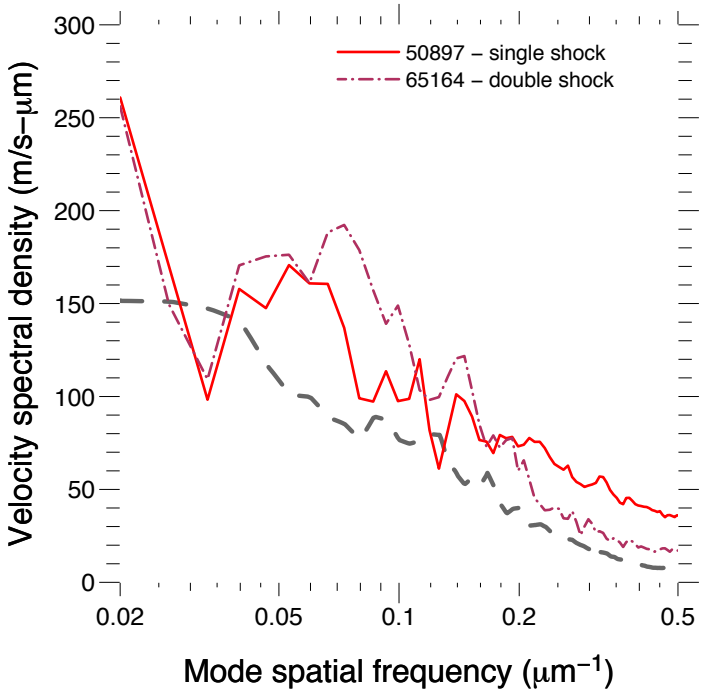

Figure 2: Velocity fluctuation spectra measured for single-shocked and double-shocked HDC ablators. The gray dashed curve represents the noise floor of the measurement (which is higher than for the measurements in Fig. 1). The fluctuation levels behind the second shock appear comparable to those behind the first shock.

Measuring the adiabatic index of polystyrene using counter-propagating shocks and x-ray Thomson scattering (HeatCap – PI: A. Pak)

A. Pak, T. Ma, L. Fletcher, T. Doppner, and S.H. Glenzer

The adiabatic index of a material, γ, is an important quantity in determining a material's equation of state (EOS), which describes the response in density and temperature of a material to a change in pressure such as that created by a strong shock. Understanding the EOS of polystyrene, a material similar to the NIF ablator, at high densities (>4x solid) and at temperatures of several eV, is of interest as it may inform the design and performance of current implosion experiments. In the CH-HeatCap campaign at Omega, the electron density, temperature and charge state of shocked polystyrene (CH) was directly measured with x-ray Thomson scattering (XRTS). Using the Hugoniot relationships for a single strong shock, γ can be experimentally determined by measuring the mass density of the shocked material. Additionally, the use of colliding shocks in this experiment allowed for γ to be measured at higher mass densities and temperatures than could be obtained using a single shock.

Figure XX a) shows the experimental setup, in which 6 drive beams on each side drove counter propagating shock waves into an initially 200 μm thick polystyrene foil. The drive beams were each 1 ns long and delayed with respect to one another to create a ~ 3 ns long pulse with a spot diameter of 800 μm at an intensity of ~ 1×10^{14} W/cm^2. An additional 8 co-timed laser beams with a 1 ns pulse width, and a focused intensity of ~ 1×10^{15} W/cm^2, created a probe of zinc He-α x-rays. The x-rays scattered through the shocked CH and to the ZSPEC crystal spectrometer onto the framing camera 4 detector. The timing of the probe with respect to the drive was varied to probe the CH before, during and after shock collision.

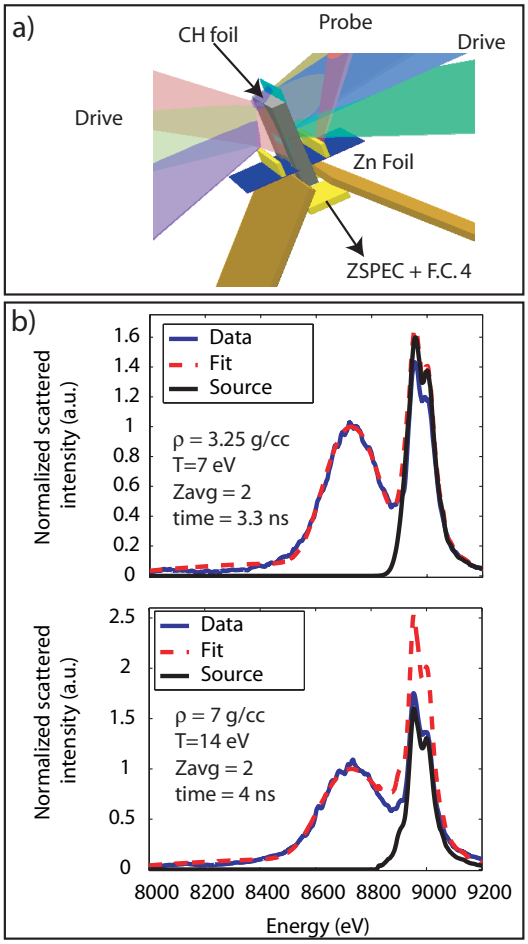

Figure XX a) Experimental setup. Two drive bundles compress the CH foil, while a probe bundle creates a burst of Zn He-α x-rays that scatter through the target. Scattered x-rays are collected via ZSPEC onto a framing camera detector in TIM 3. Fig. b) The upper and lower panel show the normalized source and scattered x-ray intensity vs. energy before and after shock collision respectively.

Figure XX b) shows the scattering spectrum at two different times, just before and after shock collision in the upper and lower panel respectively. An increase in the width of the lower energy down shifted Compton feature indicates an increase the materials electron density. Initial fits of the data indicate that a single shock density of 3.25 ± .5 g/cc and a 7 ± .5 g/cc density after shock collision has been reached. From this preliminary data analysis, the γ measured at the single and double shock density is 1.7-2.1 and 1.57-2.36, respectively. Additional data analysis is ongoing.

In a second set of experiments, this time using Omega-EP, a new experimental platform was developed to pursue similar physics. This year a total of four shot days in the BeXRTS and CH HeatCap campaigns were spent to develop an experimental platform utilizing counter-propagating shocks and x-ray Thomson Scattering (XRTS) at Omega EP. One unique property of this class of experiments is that they allow for the adiabatic index, γ, of warm dense matter (WDM) to be directly measured. Additionally, counter-propagating shocks allow for materials to be compressed to higher densities and temperatures than single shock experiments can create. A direct measurement of the γ of a material at densities and temperatures relevant to conditions existing in the ablator of NIF implosion experiments will contribute to the understanding, selection and performance in ablator materials.

The experimental setup is shown in Fig XX a). In these preliminary experiments, a 200 x 1000 x 1400 μm polystyrene (CH) foil was driven symmetrically from two sides by separate laser pulses. Each drive pulse had a wavelength of ~351 nm, a 4 ns temporal width, and an average on target intensity of ~ 1 $x10^{13}$ W/cm^2. The two drive lasers each create a strong shock that counter-propagate with respect to one another and collide at the center of the CH foil. Two additional 1 ns long UV laser beams are focused onto a zinc foil to create an x-ray probe pulse. The Zn He-α x-rays scatter from the shock compressed CH foil through a gold aperture in the bottom of the target to the HOPG ZSPEC crystal spectrometer and onto a framing camera detector that records the scattering signal over ~ 500 ps. Figure XX b) shows a XRTS spectrum obtained at 4 .5 ns after the laser drive had begun. The initial fit is in good agreement with predicted values for the density, temperature and charge state from 2D Hydra simulations at this time. Additional analysis of the data is ongoing at this time.

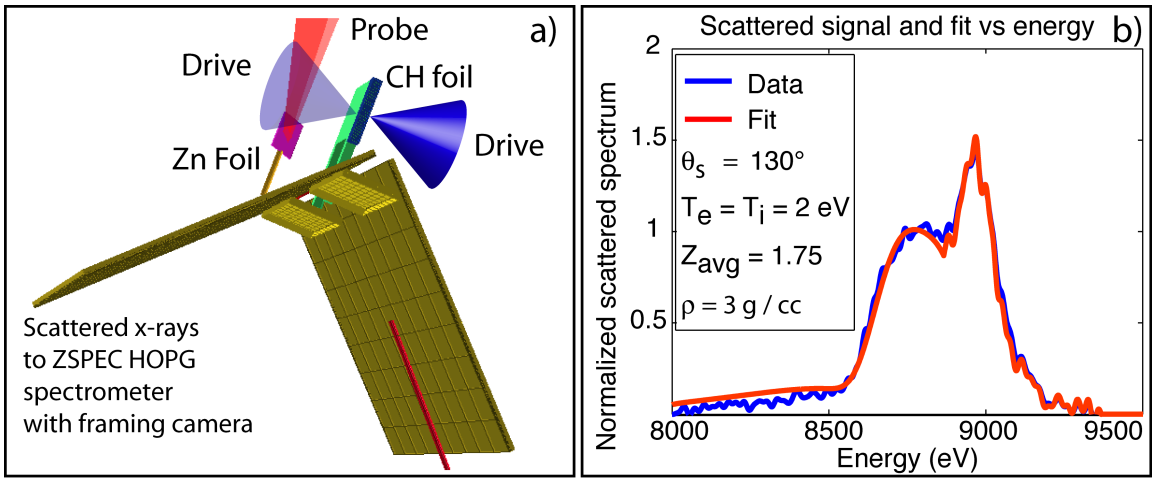

Figure XX. a) The experimental setup for the XRTS Omega EP colliding shock campaign. The CH foil is driven from the top and bottom by a separate 4 ns long UV laser pulse with I_o ~ 1 x 10^{13} W/cm^2. The counter-propagating shocks are diagnosed using Zn He-α x-rays created from one or two probe UV laser beams. The scattered x-rays travel through a target aperture to the ZSPEC HOPG crystal spectrometer and onto a framing camera. b) An example of the measured scattered x-ray signal plotted vs. energy taken at a time 4.5 ns from the start of the laser drive. Shown in red, is the fit of the scattered signal indicates that ρ = 3 g/cc, T = 2 eV and Z_{avg} = 1.75.

Ablator Opacity Measurements (AblatOp – PI: R. Heeter)

R.F. Heeter, A. Graf, G.V. Brown, C. Mauche, R.E. Marrs, and B. Wilson

A new effort was initiated in FY12 to validate models of X-ray absorption and re-emission of capsule ablator materials, including germanium, silicon, and GDP plastic, over X-ray energies and material conditions typical of inertial confinement ablation plasmas. Experiments were undertaken using two platforms. First, the HED hohlraum-based opacity platform on Omega-60 was used to assess the transmission opacity of Si, Ge, and GDP samples in LTE at T = 100 eV at densities around 0.03 g/cc. The second platform was launched in FY12 on Omega-EP, and uses dual short-pulse backlighters to measure the X-ray transmission of buried silicon layers embedded in plastic samples. This newer Omega-EP technique is able to achieve both higher densities and higher temperatures than the Omega technique, but requires tuning to achieve uniform sample conditions.

Sample data from the initial Omega-60 experiments are shown in Figure 1 (Omega-60). For both Si and Ge samples, the transmission data for the spectral band from 250-1500 eV came in below the expected transmission calculated with standard opacity models, using the plasma conditions predicted by 2-D radiation-hydrodynamic simulations. These plastic-tamped samples appear to be cooler and denser than expected, indicating either slower ablation and heating than predicted, or a substantial error in the opacity models.

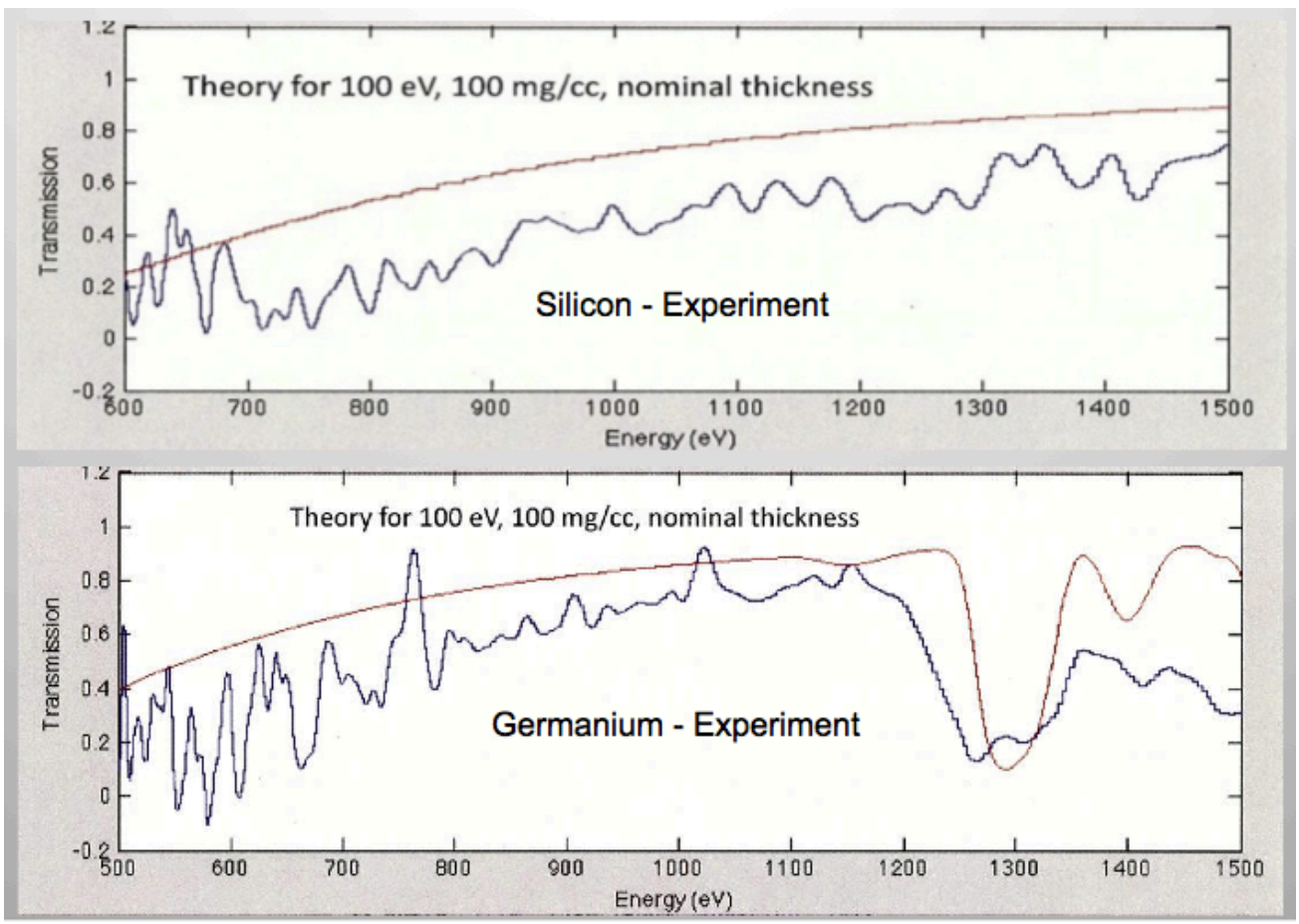

Figure 1: Initial results from silicon (top) and germanium (bottom) transmission experiments on Omega-60, with comparison to expected transmissions.

A followup shot series was completed in late FY12, including a tuned-up target design and independent characterization of the plasma conditions. Those data are currently being analyzed. Additional platform improvements, focused on reducing the noise in the transmission measurements, were implemented for beryllium-tamped Si-doped GDP (plastic) opacity shots taken in early FY13.

Meanwhile, success was also achieved in obtaining dual-axis transmission spectra for silicon samples. In this new platform, up to two of the EP UV beams are used to heat a CH-tamped Si foil with up to 200J delivered in a Gaussian pulseshape with 100 ps FWHM. Peak sample temperatures of up to 400 eV are inferred from the time-integrated emission spectra of the embedded Si foil. Shortly after the UV heating pulse, a 10 ps IR laser drives a Zn wire backlighter, producing a bright continuum X-ray source with 16 ps FWHM duration and roughly 20 um source size. This backlighter probes the expanding silicon plasma edge-on, measuring the sample expansion to yield the plasma density, and measuring the ionization state via absorption spectroscopy to provide information on the sample temperature. A second 10 ps continuum backlighter, synchronized to within 30 ps of the first, probes the sample face-on, delivering precise transmission spectral data for the measured temperature and density. Initial transmission measurements were completed in FY12 and are now being compared with theory.

Furthermore, by choosing a relatively thin tamper layer thickness, it is possible to tailor nonuniform density profiles and study the density of specific charge states as a function of position in an expanding ablated plasma. A sample of the latter data is shown in Figure 2. In this case, 100J of UV laser energy, arriving from the upper side of the image, heated the sample for 100 ps. The image was recorded roughly 400 ps after peak drive, during the cooling of the silicon plasma. The n=1 to 2 absorption features of multiple ionization states of silicon are visible on the left (lower-energy) side of the spectrum, with additional n=1 to n=3 features on the right (higher-energy) side. The data show that 400 ps after peak sample drive, lithium-like Si persists on the low-density, laser-heated side of the plasma, while the various charge states of L-shell ions (Be- through F-like) are observed deeper into the plasma at higher density. The typical density at the location of the L-shell features is about 0.1 g/cc. The laser appears not to have fully heated the carbon substrate and perhaps some of the silicon, so continuum absorption from the rear of the sample is also visible. This technique is now being applied to study X-ray ablated silicon-doped GDP ablator plasmas in FY13.

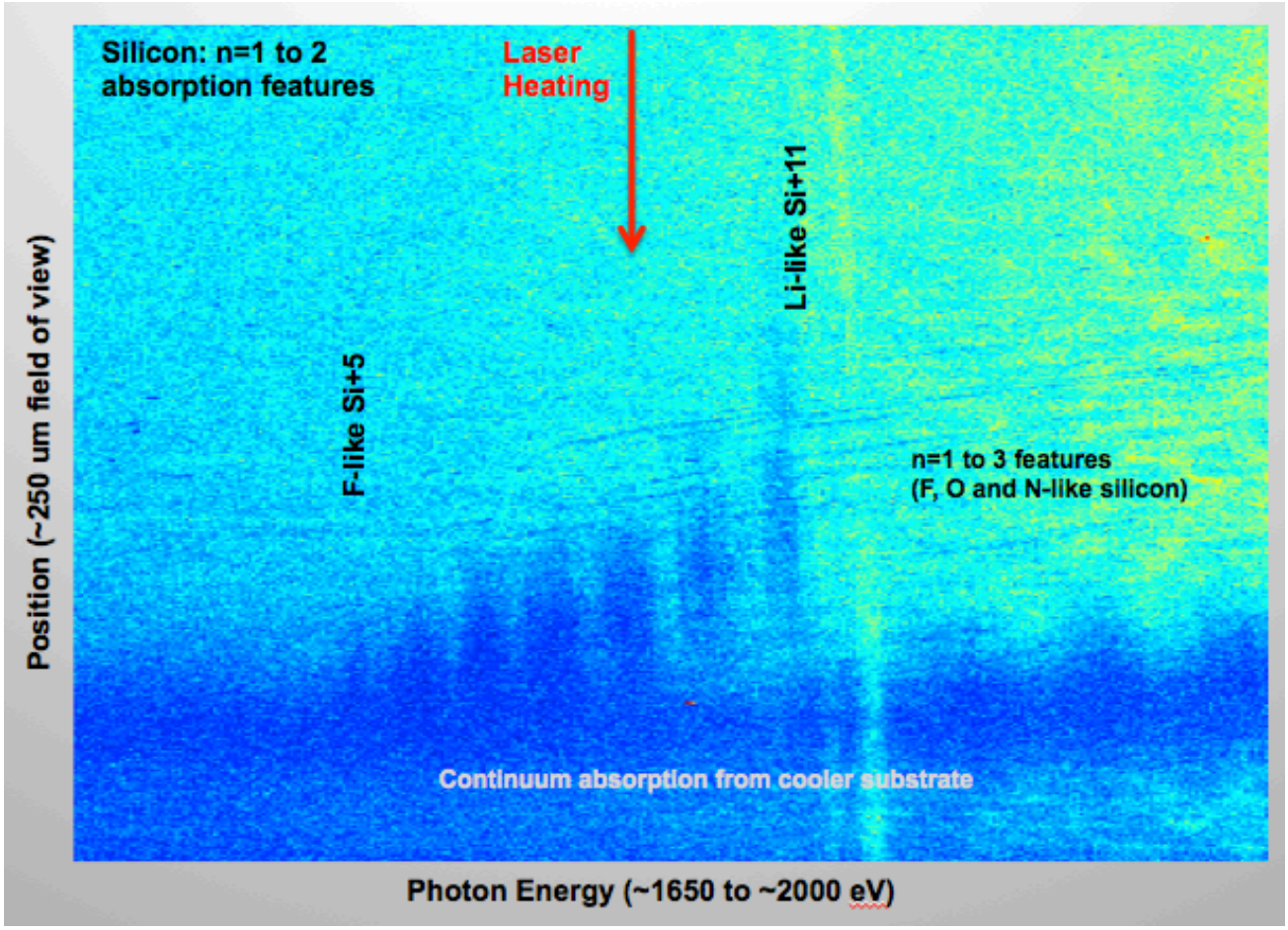

Figure 2: Space-resolved absorption spectrum obtained on Omega-EP, using edge-on broadband radiography of a silicon foil deposited on a carbon substrate and overcoated with a thin CH tamper layer.

Multi-Pump Stimulated Raman Scattering (SRSMultiPump –PI: R. Kirkwood)

The second campaign in this series was carried out to investigate the co-operative interaction of multiple beams in a cone to drive stimulated Raman Scatter (SRS). The experiments used exploding CH foil targets pre-heated by 11 heater beams to create a symmetric density profile. A normally incident seed beam was focused on the back side of the foil where it could produce SRS backscatter, with a total power waveform as shown in the 'seed beam only' case in figure 1. When, in a separate experiment, the seed beam was intersected by a cone of 2 to 6 pump beams, that were pointed to cross the seed on the front side of the foil, where the density and temperature would allow further re-amplification of the SRS, a significant enhancement in the scattered power was observed. The enhanced level of power was seen to increase with the number of pumps as expected from models of SRS re-amplification, and the total peak SRS was significantly greater than the sum of the SRS observed in both 'seed only' and '6 pumps' cases as also shown in the figure. The overall increase in SRS with all beams cannot be explained by the simulated change in absorption by the plasma due to the pump beams and has the magnitude expected for SRS re-amplification. The experiment has provided an important benchmark for models of multi-beam stimulated Raman scatter from ignition experiments.

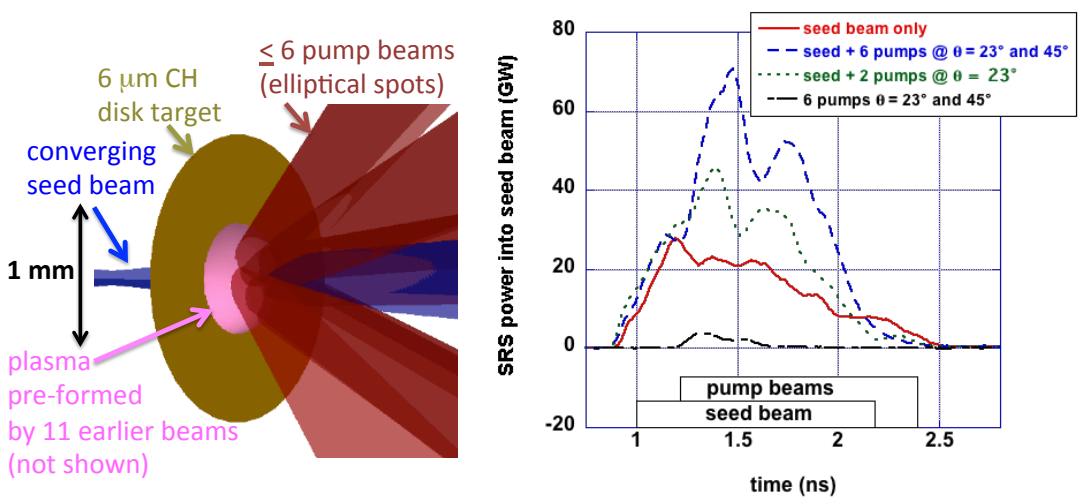

Figure 1. The geometry and measured SRS backscatter of a seed beam in the presence of different numbers of pump beams, from the SRS Multipump experiments.

Comparison of Plastic and High-Density Carbon Ablator Performance (HDCEnerg – PI: S. Ross)

The HDCEnerg-12A campaign successfully compared High Density Carbon (HDC) and CH ablator performance. A series of OMEGA 60 experiments with three distinct pulse shapes were used to investigate HDC and CH performance. The pulse shapes were designed to deliver different drive pressures during the foot of the laser pulse. The pulses delivered foot pressures ranging from ~1.7 Mb (LA234002) to ~7.5 Mb (LA190801) with an intermediate pressure of ~3.6 Mb (LA232301). The capsules were filled with either 40 atm or 20 atm of deuterium. The measured neutron yield is shown in Figure 1.

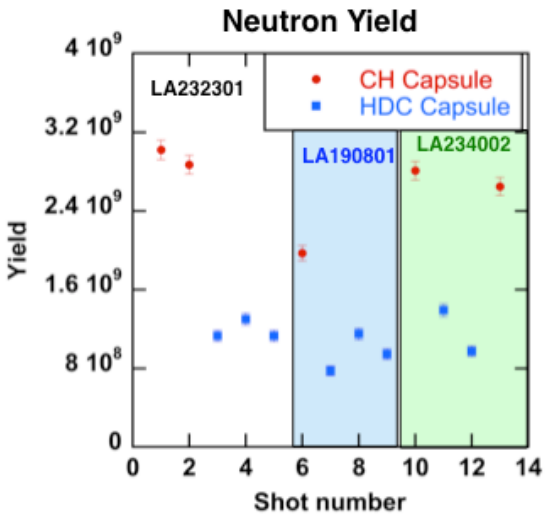

Figure 1: The measured neutron yield for different capsule materials and different pulse shapes.

The HDC capsules showed very similar neutron yields for all three pulse shapes. This is evidence that the capsule compression and performance is independent of the pressure in the laser foot for pressures ranging from 1.7 Mb to 7.5 Mb. The difference in HDC and CH yields are expected due to differences in capsule thickness. These results are being used to design future HDC experiments.

Shock Release of ICF Relevant Materials (CHD2Rel – PI: D. Fratanduono)

ICF capsule implosions on NIF are driven by four shock waves. The strength and timing of each shock is controlled in order to maintain a low adiabat. Previous high-pressure (>1 Mbar) EOS experiments on ICF ablators have been primarily limited to Hugoniot measurements. The focus of the FY12 CHD2-Release experiments is to develop a technique to measure the release isentropes of ICF relevant materials in order to better constrain the EOS of ICF relevant materials.

Experiments are performed at the OMEGA laser facility. Target design consists of a GDP (an ICF ablator) and a thin (~50 nm) silicon nitride film separated by a vacuum or gas filled gap (~250 μm) as shown in Figure 1. A strong shock (>250 GPa) is generated in the GDP ablator. When the shock breaks out of the sample and into vacuum, it releases and isentropically expands as it propagates across the gap. When the strong shock in the GDP enters the gas filled void, a weak shock is generated and propagates across the gap. By measuring the shock state of the gas, a point on the GDP release isentrope is determined. The released material stagnates upon the silicon nitride. The velocity of the silicon nitride is measured using a Velocity Interferometer System for Any Reflector (VISAR). Using the measured velocity profile, a momentum balance technique is employed to extract information regarding the release isentrope.

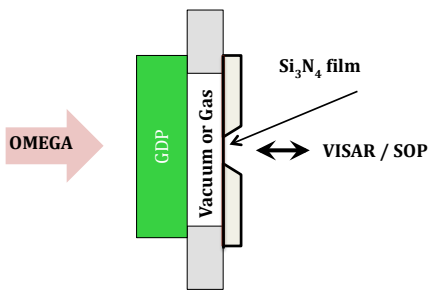

Figure 2: Target Design

The vacuum results indicate that the velocity of the leading edge of the release isentrope is traveling ~30% faster than predicted by the LEOS tables. This behavior has been observed on CH, GDP and diamond. These results are shown in Figure 2. The gas (methane) filled results are consistent with Hugoniots generated from LEOS tables. However, those at lower pressure shock states are inconsistent with the vacuum measurements. Further experiments are being performed to examine this discrepancy. We are in the process of designing targets to measure the release of D_2 ice into low density D_2 gas. Using this technique, we may be able to determine species separation for DT.

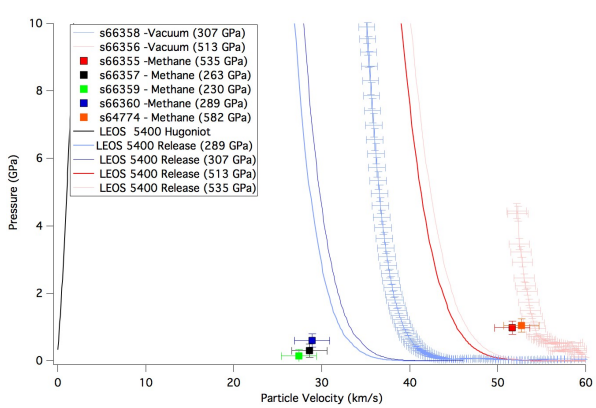

Figure 3: GDP Release Isentropes

High-Energy-Density Experiments

I. Material Dynamics and Equation-of-state

Tantalum Rayleigh-Taylor Experiments (ICETaRT-12, PIs Hye-Sook Park and Chris Plechaty)

The focus of the ICETaRT campaign was to study Ta material strength at high pressure (> 1 Mbar), and high strain rates (10^6- 10^8 s^{-1}). To achieve these conditions in the experiment, while keeping the temperature of the Ta sample well below melting, a reservoir and vacuum gap (Park 2010a) configuration was employed to produce a quasi-isentropic pressure drive (figure 1). The plasma drive was produced by heating a hohlraum with 40 Omega beams, depositing a total energy of 20 kJ. Attached to the side of the hohlraum was an ablator/reservoir and a physics package, which were separated by a vacuum gap to produce ramped drive conditions onto the physics package.

The physics package consisted of a CH heat shield placed on a Ta sample. Imposed on the surface of the Ta were sinusoidal perturbations. In the experiment, as the plasma from the reservoir crosses the gap and stagnates on the sample package, the Ta ripples undergo an effective acceleration from the stagnating plasma drive. This acceleration actuates Rayleigh-Taylor (RT) growth of the pre-imposed sinusoidal pattern. Since the Ta material strength acts to suppress the amount of RT growth, measuring the RT ripple amplitude gives a measure of the material strength (Barnes 1973, Park 2010a, Park 2010b). To measure the perturbation amplitude, face-on high energy (22 keV Ag k-α) radiography was employed using an EP short pulse beam. We needed the EP beam to employ a high energy backlighter (22 keV) to probe the high-Z tantalum material. The amount of backlighter transmission through the ripples is governed by the quantity $\rho\Delta Z$, where ρ is the density of the driven ripples and ΔZ is the amplitude. The RT growth factor GF is determined by measuring the driven $\rho\Delta Z$ (Park 2010a, Park 2012):

$$GF = \frac{(\rho\Delta Z)_{driven}}{(\rho_0\Delta Z_0)_{undriven} \cdot MTF}$$

where ρ_0, ΔZ_0 are the initial density and ripple amplitude (determined from pre-shot metrology) and the MTF is the modulation transfer function, which characterizes the frequency response of the system and is measured by using a knife edge technique. In order to determine the properties of the plasma drive, separate shots without the backlighter were performed by replacing the physics package with a witness sample and taking VISAR measurements.

The FY 2012 ICETaRT campaign employed the experimental setup discussed above to study several aspects of Ta material strength. The first topic studied was the Ta material failure threshold. In previous experiments, we observed (figure 2) that as the relative growth increases, defined as the ratio between the ripple amplitude and the Ta sample thickness, the measured relative growth deviates from that predicted by the multiscale model (Barton 2011). To study the threshold where the relative growth measured in experiments deviates from that predicted by the multiscale model, or measure the threshold where failure occurs, a three-amplitude ripple pattern was employed. The Ta sample was split into three regions, each with the same wavelength of 50 μm, but with different amplitudes – namely 1.0, 2.0, and 3.5 μm. We found that failure occurred as the relative growth in the experiment exceeded ~20 %.

The second topic studied was a comparative material strength study between Ta [100] and Ta [111] crystal orientations. In previous studies (Park 2012a) the target samples were predominantly in the [111] orientation. In the multiscale model, crystal orientation can affect material strength via the Taylor factor. To understand the effect of crystal orientation on the material strength, we placed the two samples side-by-side and compared the ripple growth for a given shot (in figure 3). Initial results from just a few

shots suggest that the difference in the growth factor between these two crystal orientations is too small to be measured within our error bars of ~18%.

Lastly, the final topic of study undertaken in the FY 2012 ICETaRT campaign was the study of a new multimode configuration (figure 4). In this experiment, a superposition of two different sinusoidal ripple patterns was imposed on the Ta sample. The two modes employed had the same amplitude (1.85 μm), but different wavelength (75 and 112 μm, respectively) and phase (210 and 24 degrees, respectively). The purpose of this study was twofold. The first purpose was to study the coupling of RT growth between the modes. For example, the growth of the designed modes with wavevectors k_1 and k_2, induce growth at $|k_1 \pm k_2|$, $2k_1$, and $2k_2$. The exact details of the coupling are not fully understood. Second, by using multiple modes, the multimode configuration can be used to produce simultaneous RT measurements, with corresponding strengths. A careful and detailed analysis of this data is currently underway.

References:

Barton, N.R., *et al*., J. Appl. Phys., **109**, 073501 (2011).
Park, H.S., *et al*., Science (Submitted 2012a) .
Park, H.S., *et al*., Phys. Rev. Lett., **104**, 135504 (2010).
Park, H.S., *et al*., POP, **17**, 056314 (2010).
Barnes, J. F., *et al*., J. Appl. Phys. **45** (2), 727, (1974).
H.-S. Park, et al., AIP Conf. Proc. **1426**, 1371 (2012)

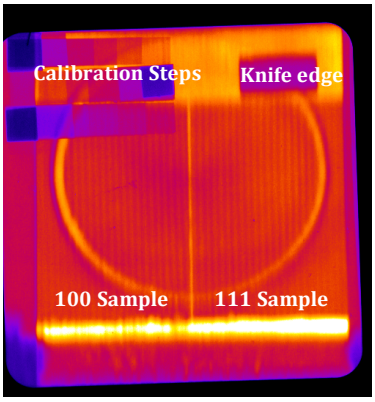

Figure 3. Radiography image of [100] and [111] target configuration. The 100 sample is on the left, and the 111 sample is on the right. The calibration steps are employed to relate the backlighter transmission to a specific value of rDZ. The knife edge is used to determine the MTF. The circular structure in the middle is a hole in the hohlraum and indicates where the plasma drive can stagnate onto the

Iron Rayleigh-Taylor Experiments (ICE-Iron-RT-12, PI Chris Plechaty)

The ICEIronRT campaign focused on the study of iron material strength at high pressures and strain rates when a phase transition occurs at lower pressures (~100 kbar). The goal was to understand the strength parameter difference at high pressure when a phase transition occurs from the α to ε phase at a lower pressure level.

For ICEIronRT, we employed a quasi-isentropic plasma drive produced by a reservoir-gap-sample configuration (Park 2010). A newly designed 6% BrCH reservoir was employed to achieve pressures up to ~1.5 Mbar. In the experiment, 40 Omega beams (total energy of 20 KJ) were employed to ablate a hohlraum with a side-mounted reservoir-gap-sample package, to produce a plasma drive. As the plasma drive crossed the vacuum gap, it stagnated onto the Fe sample with an imposed sinusoidal pattern on the surface. The stagnation of the plasma drive onto the Fe sample drives Rayleigh-Taylor (RT) growth of the ripples where the observed RT growth rate is dependent upon the strength.

To obtain the quantities listed in (1), $\rho_0\Delta Z_0$ was derived from pre-shot Veeco measurements, and the MTF was measured using a knife edge technique (Figure 1). To measure $\rho\Delta Z$ for the driven sample, face on high energy (22 keV) radiography was employed using an Ag micro-flag backlighter (200×200×5μm). A short pulse (100 ps) EP beam was employed to ablate the backlighter with a 1.0 KJ pulse delivered with a given time delay in respect to the Omega drive beams. To resolve the ripple growth, the thinnest side of the backlighter was aligned along the direction of the ripples.

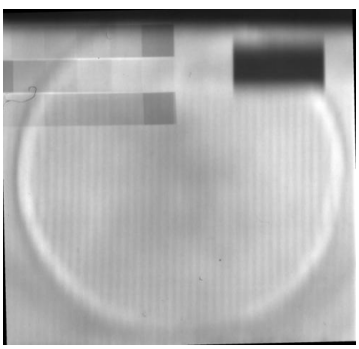

Figure 4: A radiograph for shot 67210 (60 ns delay) In this radiography image, the iron calibration steps are located in the left-hand corner, and are used to relate the backlighter transmission to a specific value of $\rho\Delta Z$. The knife edge is located in the right hand corner, and is used to measure the MTF. The circular feature in the middle of the image indicates the region of driven ripple growth.

In addition to joint Omega-EP shots, Omega-only shots were performed to determine the properties of the plasma drive. In these shots, the Fe sample was replaced with a witness sample and VISAR measurements were performed.

In figure 2, we show a comparison between the undriven ripple $\rho_0\Delta Z_0$, and the driven ripple $\rho\Delta Z$. As shown, $\rho\Delta Z$ is greater than $\rho_0\Delta Z_0$, indicating that the driven ripples have undergone RT growth. The GF, calculated with equation (1), is shown in figure 3 with error bars of ~±50%. An initial analysis indicates that the iron material strength is higher than that predicted using a hybrid α to ε phase transiting

PTW strength model (Belof 2012) -- calculated using our experimental condition of ~1.5 Mbar pressure and strain rate >10^6 s^{-1}.

References:

J. Belof et al., AIP Conf. Proc. 1426, 1521, 2012
Park, H.S., et al., Phys. Rev. Lett

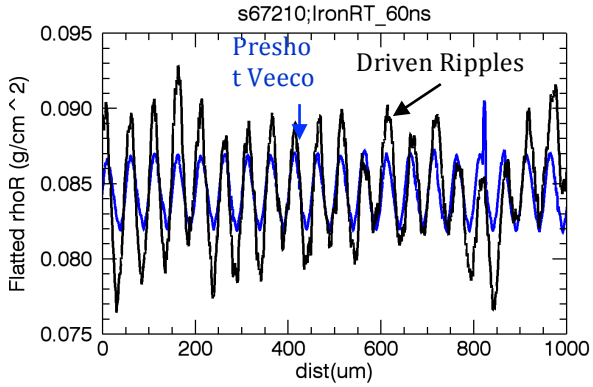

Figure 6. Comparison of the pre-shot values of $\rho_0\Delta Z_0$ and the shot values of $\rho\Delta Z$ for a 60 ns delay between the Omega drive and EP backlighter beams.

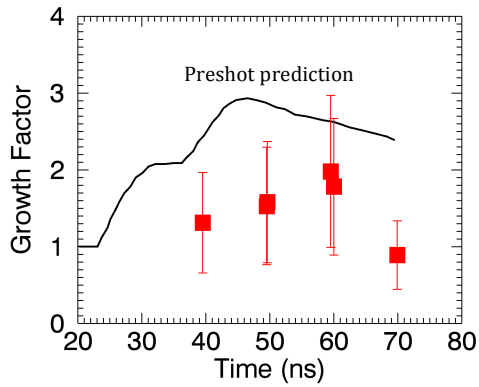

Figure 6: Comparison between the GF (with error bars of 50%), and the GF prediction obtained from a hybrid α to ε transition PTW model.

Double-Pulse Radiography Development (DblPulse-12, PI Chris Plechaty)

Laser-driven high-energy (>22 keV) X-ray radiography has been employed as a diagnostic tool in many different types of HED experiments, with applications ranging from material strength studies (Edwards 2004, Park 2006, Park 2010a,b) to capsule implosion experiments. In FY 2012, the DBLPULSE campaign focused on the development of a new multi-frame radiography technique that takes advantage of the multiple beams available at state-of-the-art laser facilities such as Omega and the National Ignition Facility (NIF). This concept is of particular importance to the NIF and HED programs since it will yield twice the amount of data per shot.

Experiments were performed at the OMEGA/EP laser facility utilizing two short pulse (100 ps, 100 µm spot size) beams to independently ablate two 300×300×10 µm foils (Cu and Ag) placed 1.2 mm apart (figure 1). In the experiment, a 1 kJ beam was employed to ablate the Cu backlighter. After a delay time *t,* the Ag backlighter target was irradiated by a 1.5 kJ beam. The performance of the two time-delayed x-ray pulses were tested by radiographing an Au grid pattern placed 10.3 mm from the foils. To obtain two distinct images of the grid pattern, a collimator was employed. The collimator consisted of a 1 mm thick Au disk, with two tapered holes to act as pinholes for each backlighter. The surface of the collimator was placed 3.2 mm from the center of the foils. The angle of the holes was chosen such that two distinct and spatially separate images were produced at the location of the Image Plate (IP), placed ~500 mm from the foils.

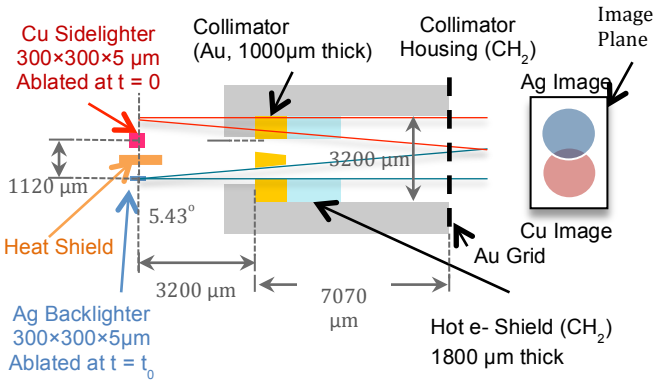

Figure 7: Schematic of Experimental Setup. In experiment, X-rays from the two independently ablated backlighter foils passes through a collimator assembly. This produces two temporally and spatially independent images of an Au grid on an image plate.

To characterize the frequency response of the system, the Au grid pattern employed consisted of several orthogonal mesh elements, each with different spatial scales. The Au grid had 10, 20, 30, 40, and 80 µm mesh features, aligned along the horizontal and vertical axes of the grid. The Cu and Ag foils were mounted orthogonal to each other and the IP, such that each backlighter would produce a 1-D orthogonal x-ray source aligned along either the vertical or horizontal axis of the Au grid. The IP was placed far enough away so that two spatially distinct images were captured.

To protect the second backlighter target from the hydrodynamic expansion and x-ray emission from the first backlighter, a heat shield was placed between the foils on a separate target positioner.

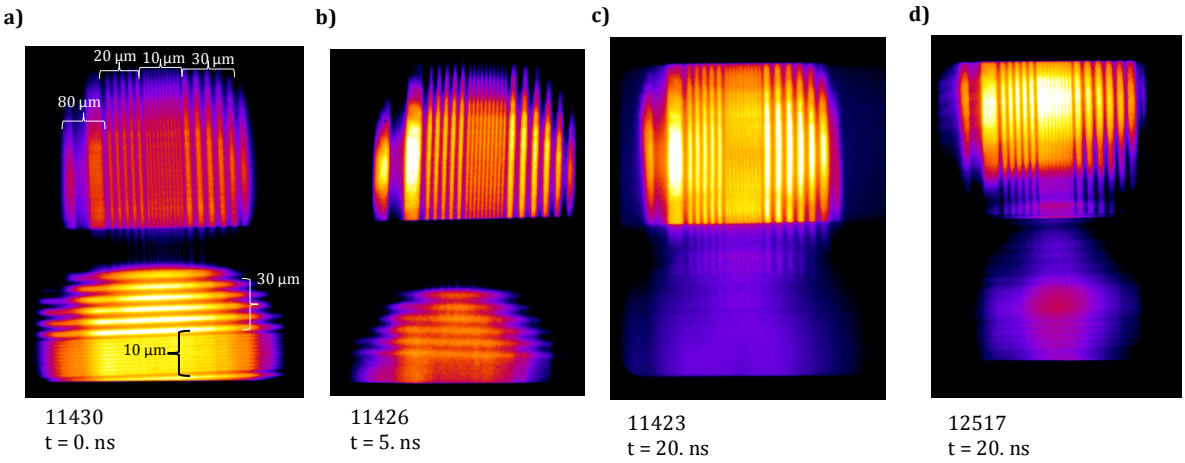

Figure 8: Images obtained with the HERIE. In these images, the top image is produced by the Cu backlighter, which is always taken at $t = 0$ ns. The bottom image produced by the Ag backlighter, which ablates the foil at the time shown. In a)-c), a 1000×1000×200 µm thick CH heat shield was employed. In d) a 1000×1000×50 µm thick Au heat shield was employed.

Radiography images captured using this configuration are shown in figure 2. In figure 2a-c, the heat shield employed was a 1000×1000×200 µm thick CH heat shield. At t = 0 ns (figure 2a) the 10, 20, 30, and 80 µm features are clearly visible in the Cu (top) image. In the Ag (bottom) image, the 10 and 30 µm features are observed, while the other features are located out of the instrument field of view. At t = 5 ns (figure 2b), the image produced by the delayed backlighter is observed to degrade; only the 30 µm features are visible. This trend continues when t = 20 ns (figure 2c), where the Ag backlighter resolution has degraded enough such that the grid features were not observed.

An explanation for the reduction in the image quality can be found by examining the time-integrated x-ray Pinhole Camera (XRPHC) images (figure 3). As shown by figure 3, the Ag backlighter x-ray source size becomes notably larger for the t = 20 ns case (figure 3c) when compared to the t = 0 ns case (figure 3b), causing the delayed image quality to degrade.

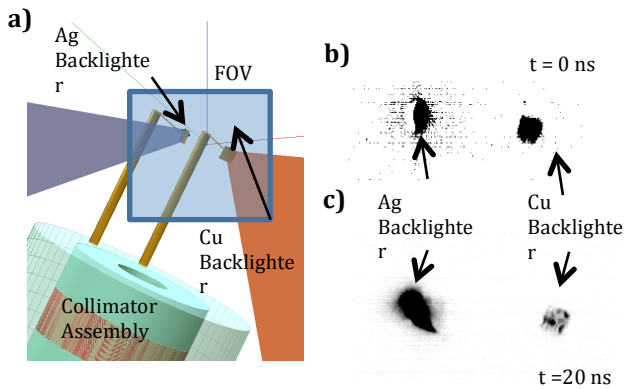

Figure 9: XRPHC Images: a) Image geometry showing the Cu beam and backlighter (on the right), and the Ag beam and backlighter (on the left). The field of view (FOV) for the XRPHC images is shown. The time-integrated images captured are shown in b) for the case of t = 0 ns, and c) for the case of t= 20 ns.

Since the CH heat shield employed for the images captured in figure 2a-c is transparent to laser backscatter, and x-ray emission from the t = 0 ns backlighter, it was replaced by a 1000×1000×50 µm Au heat shield (figure 2d). When employing this heat shield design, the resolution of the delayed backlighter only slightly increases. Employing an even thicker Au heat shield (1000×1000×200 µm) does not yield better system resolution.

Since the 50 µm thick and 200 µm thick Au heat shield prevents a significant portion of the low energy x-ray emission from the Cu backlighter from reaching the Ag backlighter, the observed preheating of the Ag backlighter is likely caused by radiating plasma expansion. As the Cu backlighter is ablated, the resulting plasma expands past the heat shield and radiates. This causes the Ag backlighter to be pre-heated, producing plasma and increasing the x-ray source size once the backlighter is ablated. A future study will investigate this effect.

References:

Edwards J., *et al*., Phys. Rev. Lett. **92**, 075002 (2004).
Park, H.S., *et al.*, Phys. Rev. Lett. **104**, 135504 (2010).
Park, H.S., *et al.*, Phys. Plasmas **17**, 056314 (2010).
Park, H.S., *et al.*, Phys of Plasmas, **13**, 056309 (2006).

Diffraction Studies on Shocked Tantalum (PIs B. Maddox, A. Comley and C. Wehrenberg)

Four distinct experiments were conducted to study the behavior of shocked and ramp-loaded tantalum.

StrDiff-12

The goals of the StrDiff-12A campaign were to: observe twin formation in single crystal Ta shocked along the [110] direction, obtain large-pinhole diffraction for a quantitative temperature analysis of shocked Ta, extend previous measurements of the lattice anisotropy of Ta shocked along [100] to lower peak pressure, verify simulations using a stepped diamond drive target, and to test a glue-less target for future studies of shock- and ramp-compressed Ta. The experiment used the BBXRD on TIM4 as the primary diffraction diagnostic, as well as the tilted VISAR. Crystal samples were driven using a single beam (Beam 18) with an SG8 phase plate. The x-rays for diffraction were produced by an imploded CH shell driven by 44 beams with SG4 phase plates. All beams used a 1 ns square pulse. We achieved 12 shots and obtained excellent data. Due to the initial crystal sample quality of the Ta [110] samples, we were unable to observe any useful driven diffraction patterns for Ta shocked along [110], and thus observed no twinning. However, all other experimental goals were met. In this campaign, we recorded our highest quality Laue diffraction pattern to date, detecting up to 7 compressed diffraction spots on a single side of the BBXRD detector (shown in Fig. 1)

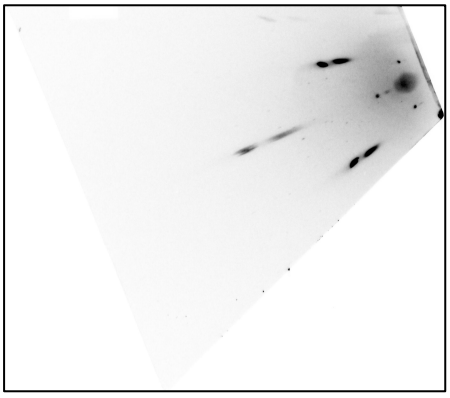

Figure 1. Example of high-quality Laue diffraction recorded from Ta single crystal shock compressed to ~0.5 Mbar along the [100] direction

TaRDIff-2012

In TaRDiff-2012 our goal was to study twinning and dislocation motion in shock compressed tantalum. The experimental configuration used the BBXRD on TIM4 as the primary diagnostic for studying twinning. Alternatively, a recovery tube was fielded on TIM1, to allow study of recovered micro-indented samples. Samples were driven using a 1ns square pulse with laser energy in the 15-65J range. High quality diffraction data was obtained and Ta samples were successfully recovered. Initial analysis did not show driven diffraction signal for (110) Ta samples, which were expected to show larger amounts of twinning. However, high contrast driven Laue spots were observed for (100) oriented Ta crystals, and this data was used in Ta strength measurements. Recovered Ta samples will be examined by TEM to measure the dislocation motion originating from the micro-indents.

ShkLaue-2012

In ShkLaue-2012 our goal was to extend previously successful strength measurements of shocked Ta using in-situ Laue diffraction to ramped-loading conditions, allowing comparison to Rayleigh-Taylor strength experiments with similar strain rates. As in previous ShkLaue campaigns, the BBXRD diagnostic was used to record Laue diffraction data, giving a direct measurement of lattice anisotropy and

shear strength of the material. A reservoir drive was developed in which a directly driven brominated-CH reservoir releases across a gap and creates a ramped stagnation shock on the Ta sample. A new glueless target design was also developed for this campaign, in which the Ta samples were kept on the MgO substrate and the substrate is polished down to the desired thickness. This design allowed us to record high-quality VISAR data simultaneously with Laue diffraction data. Initial analysis shows that the reservoir drive was successful in creating the ramped drive, which demonstrated highly repeatable behavior. High contrast diffraction data was recorded for a range of drive times, and these data show a range of lattice anisotropy ratios.

EP-TaBragg-2012

In TaBragg-2012 our goal was to study shock compressed Ta using in-situ Bragg diffraction, building on the successful BraggDiff-2011 campaign. The experimental configuration used the Lawrence Livermore Diffraction Imager as the primary diagnostic on TIM13. Samples were driven using two defocused beams with a 10 ns pulse, while a short pulse beam was used to drive a silver backlighter to create the high-energy x-rays. There were a few issues in adjusting the drive-backlighter relative timing, producing an imbalance in the signal strength in either the driven or static diffraction signal in the initial shots. This issue was solved by comparing VISAR data with previous campaigns, resulting in a 0.5 ns shift from previous experiments. The data quality obtained was excellent and, combined with BraggDiff-2011 data, provides a range of pressures for Ta strength measurements.

Ta X-Ray Diffraction (PIs A. Lazicki, J. Eggert and R. Rygg)

Powder x-ray diffraction experiments on solid ramp-compressed tantalum in FY12 yielded additional data points confirming a high pressure phase transition near 300 GPa. The structure was determined to be consistent with a predicted simple hexagonal (omega) phase[1]. During the shot day, Ta and Fe samples were ramp compressed to pressures above 10 Mbars. The technical difficulties encountered while trying to measure x-ray diffraction at these high pressures have provided critical feedback for the design of terapascal-range x-ray diffraction experiments on the NIF

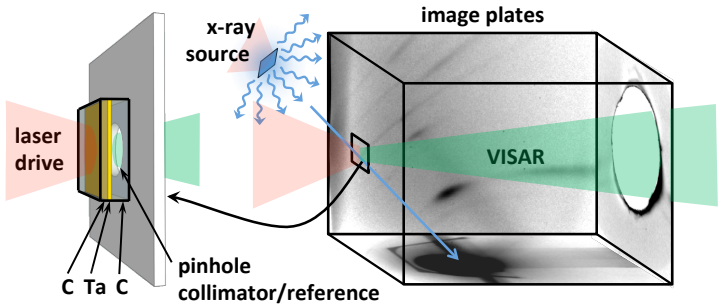

Figure 1. X-ray diffraction experimental set-up. The target consists of a 4 micron foil of Ta sandwiched between single-crystal diamond plates. The x-ray source is the laser-excited helium-alpha radiation from Fe or Cu thin foils. X-rays diffracted off of the Ta sample are scattered onto the inner surfaces of a box lined with image plates, yielding crystal structure and volume. Target rear surface velocities are detected using VISAR, yielding pressure.

Figure 2 Shift of the d-spacings of x-ray diffraction peaks under pressure, showing evidence of a new phase at 300 GPa.

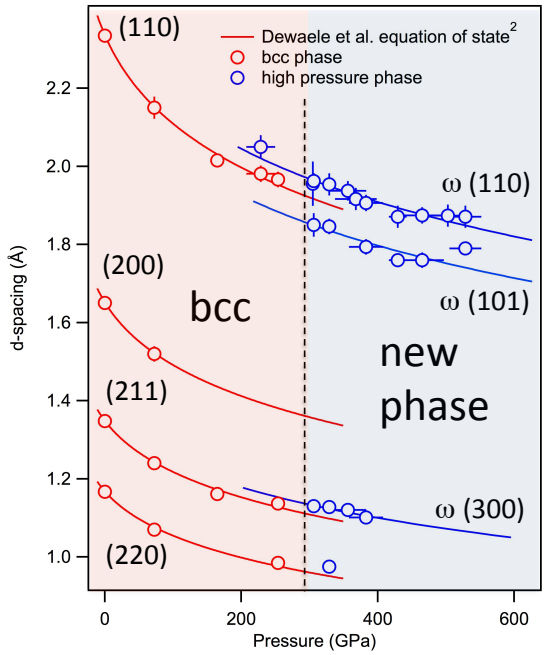

[1]Burakovsky et al., Phys. Rev. Lett. **104**, 255702 (2010).
[2]Dewaele et al., Phys. Rev. B **70** 094112 (2004).

Hydrogen Equation of State (PIs Amy Lazicki, Marius Millot, Ryan Rygg and Jon Eggert)

The purpose of this study was to look for pressure-induced chemistry in deuterium by electron doping from an added ~5% Xenon, evidenced by the effects on the Hugoniot and the reflectivity, compared to pure deuterium. Gas mixtures were precompressed to fluid deuterium density in a diamond anvil cell prior to shock compression. Measurements reveal a Hugoniot shifted to higher density, but not to the extent predicted by a simple linear mixing model, indicating chemical interaction between the species. There is however some uncertainty in the concentrations of gas captured in the diamond cells, so the conclusion awaits further experiments. Due to difficulties in sample preparation, some of the shots were devoted instead to measurement of the Hugoniot of the hydrogen compound lithium hydride, precompressed to 5-9 kbar in a diamond anvil cell. Results will aid in refinement of equation of state models.

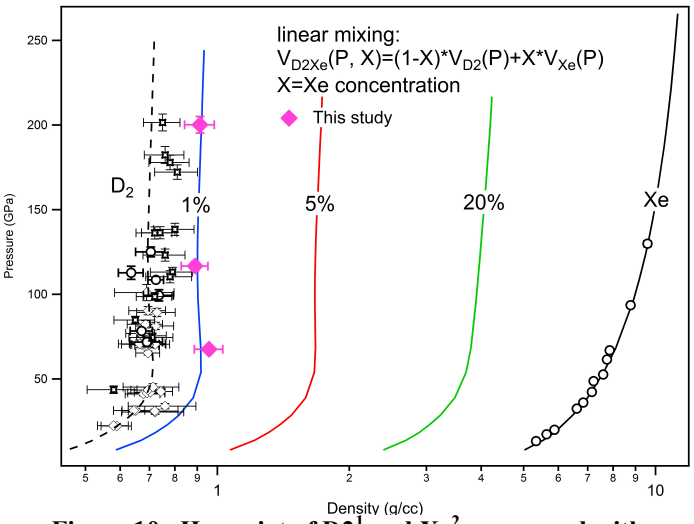

Figure 10. Hugoniot of D2[1] and Xe[2], compared with the data from this study. Curves predicting the behavior the mixture are based on the linear mixing model.

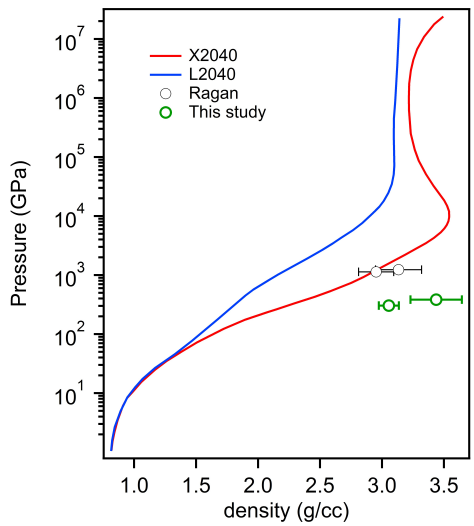

Figure 2. Hugoniot of LiH from equation of state models, compared to experimental data[3]. The data shown from this study is for LiH precompressed to ~6.5 kbar.

[1]Hicks et al., Phys. Rev. B **79**, 014112 (2009); Knudson et al., Phys. Rev. B **69**, 144209 (2004).
[2]Root et al., Phys. Rev. Lett. **105**, 085501 (2010).
[3]Ragan et al., Los Alamos report LA-UR-83-2081 (1983).

XAFS study of ramp compressed Fe, Ta and Mo

Y. Ping, F. Coppari, D. G. Hicks, B. Yaakobi, D. E. Fratanduono, S. Hamel, J. H. Eggert, J. R. Rygg, R. F. Smith, D. C. Swift, T. R. Boehly, and G. W. Collins

EXAFS measurements of dynamically compressed iron have been performed on the OMEGA laser with an implosion backlighter. Iron is compressed in the solid state to 560 GPa (5.6 Mbar), the highest solid-state pressure for iron explored in the laboratory. EXAFS (extended x-ray absorption fine structure) measurements provide simultaneous density, temperature and local-structure data for compressed iron in this new regime, the first such data for constraining solid state theory and evolution models for many newly discovered extra-solar terrestrial planets. The data show that the close-packed structure of iron is stable up to 560 GPa, the temperature at peak compression is significantly higher than expected from pure compressive work, and the strength of iron many times greater than expected from lower pressure data (Ping et al. submitted to Phys. Rev. Lett.).

Based on the success of EXAFS measurements of iron, we have extended this platform to study L-edges of Ta and Mo. Data on Mo at ambient conditions, 2Mbar and 3Mbar have been obtained, and EXAFS of undriven Ta has been observed for the first time on OMEGA. The last campaign in Sep. 2012 demonstrated 2x enhancement in backlighter brightness, and 4x enhancement in the spectrometer efficiency, making it possible to do single-shot EXAFS measurements of driven Ta in FY13.

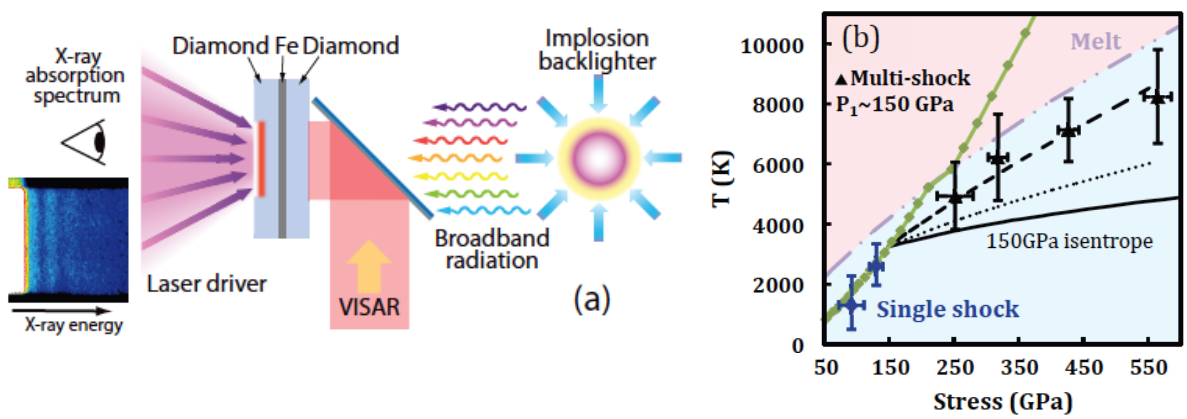

Figure 1: (a) Experimental schematic. The raw image of a typical x-ray absorption spectrum is displayed at the left-lower corner, showing the intensity modulations above the K-edge. (b) Temperature inferred from EXAFS data as a function of stress for the shock+ramp data with an initial shock of 150 GPa. The single-shock data are also shown (blue diamonds). The melting curve (dot-dot-dashed lines) and the Hugoniot (green solid lines with dots) are plotted for comparison. Also shown are isentropes (solid lines), isentropes with the temperature increase calculated using static strength Y_{sta} (dotted lines) and dynamic strength $Y_{dyn} = 3Y_{sta}$ (dashed lines).

Tin Melt (TinMelt-12, PI Amy Lazicki)

Campaigns investigating the high pressure solid crystal structure and probing the melting curve of tin have continued in 2012, extending the measured diffraction up to 720 GPa, and potentially yielding information about the melting curve up to 300 GPa. The new x-ray diffraction data provide further evidence for a high pressure-high temperature phase transition near 200 GPa. The structure of this new phase differs from the hexagonal close-packed structure that arises near 200 GPa at ambient temperature[1]. We propose the simple hexagonal omega phase as a likely crystal structure for this new phase. The particle velocity histories of shock-melted and ramp-compressed tin show a plateau consistent with changing sound velocities at a phase transition such as recrystallization. Assuming recrystallization, a preliminary analysis shows the melting temperature rising steeply with pressure, in qualitative agreement with recent diamond anvil cell results[2].

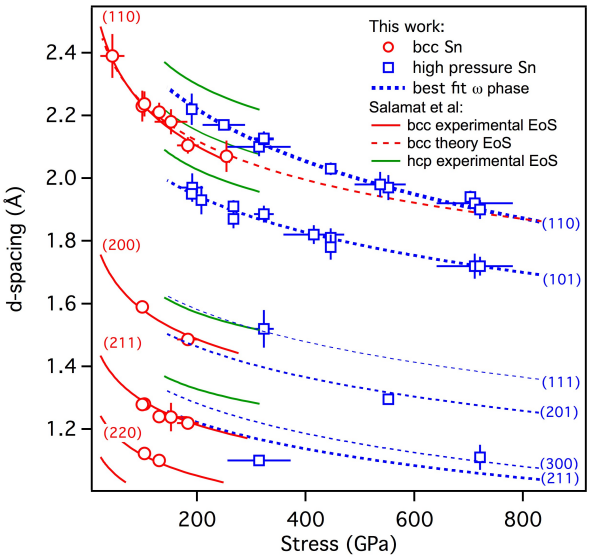

Figure 11. d-spacing of observed peaks, compared with known isothermal equation of state and phase transition from static experiments[1,4]. Our observed high pressure d-spacings fit a simple hexagonal (omega) phase. The line weight is proportional to the expected relative peak intensity.

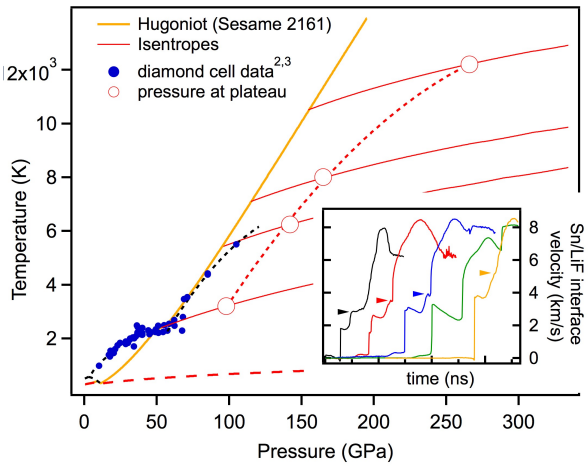

Figure 2. Melting curve of tin with new data from this study, determined from the pressure at which a plateau is seen in the ramp compression wave profile (shown in the inset). Paths in phase space are approximated as shown, with the temperatures associated with the principle Hugoniot and subsequent ramp-compression pathways (modeled as isentropes) determined from the Sesame 2161 table.

[1]Salamat et al., Phys. Rev. B **84**, 140104(R) (2011).
[2]Briggs et al., J. Phys.: Conf. Ser. **377**, 012035 (2012).
[3]Schwager et al., J. Chem. Phys. **133**, 084501 (2010); Weir et al., J. Appl. Phys. **111**, 123529 (2012).
[4]Desgreniers et al., Phys. Rev. B **39**, 10359 (1989).

Gigabar Equation of State (GbarEOS-12, PI James Hawreliak)

High pressure equation of state experiments using convergent compression of a solid spherical target have a geometric advantage over conventional planar techniques, in which a constant ablation pressure causes the propagating shock to maintain a constant pressure, because in the converging case the shock will increase in strength as it approaches the sphere's center. This approach allows the achievement of shock pressures >100 Mbar on the Omega laser facility. These experiments use in situ gated radiography to measure the propagating shock speed and density. We will apply the Hugoniot relations to determine the pressure based on the measure shock front speed and density,

$$P = \rho_0 u_s^2 (1 - \frac{\rho_0}{\rho})$$

$$\frac{\delta P}{P} = \sqrt{\left(\frac{2\delta u_s}{u_s}\right)^2 + \left(\left[\frac{\rho_0}{\rho - \rho_0}\right]\frac{\delta\rho}{\rho}\right)^2}$$

where ρ_o is the initial density and $\delta u_s, \delta\rho,$ and δP are the associated uncertainties in the shock speed, density and pressure, respectively. Figure 1 is an example of a single frame from a radiograph image from which the density profile can be inferred.

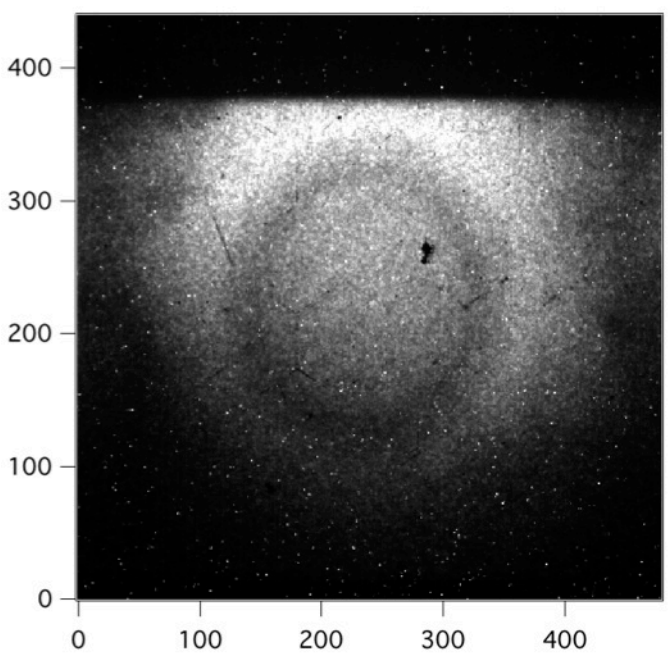

Equation of State for Foams Using Omega-EP (EP-Foam-12, PI James Hawreliak)

The equation of state of porous materials is of great interest in HED science because it allows conventional shock techniques to achieve different themodynamic end states than the principal Hugoniot. Figure 1 is an example of the pressure density space of shock-compressed quartz for a range of different initial densities. For the low density foam materials, where the final density is below the ambient density of the base material, the pressure is dominated by the thermal pressure caused by compressing the voids in the material. Many carbon based foams are opaque, unlike transparent foams where the shock front becomes reflective at high pressures and velocity can be measured directly. The opaque materials require an x-ray technique to view the shock. We are developing an in situ radiograph technique to make hugoniot EOS measurements of shock compressed opaque low density foams. We had success using a chlorinated plastic (PVC) area backlighter for 50 mg/cc CRF.

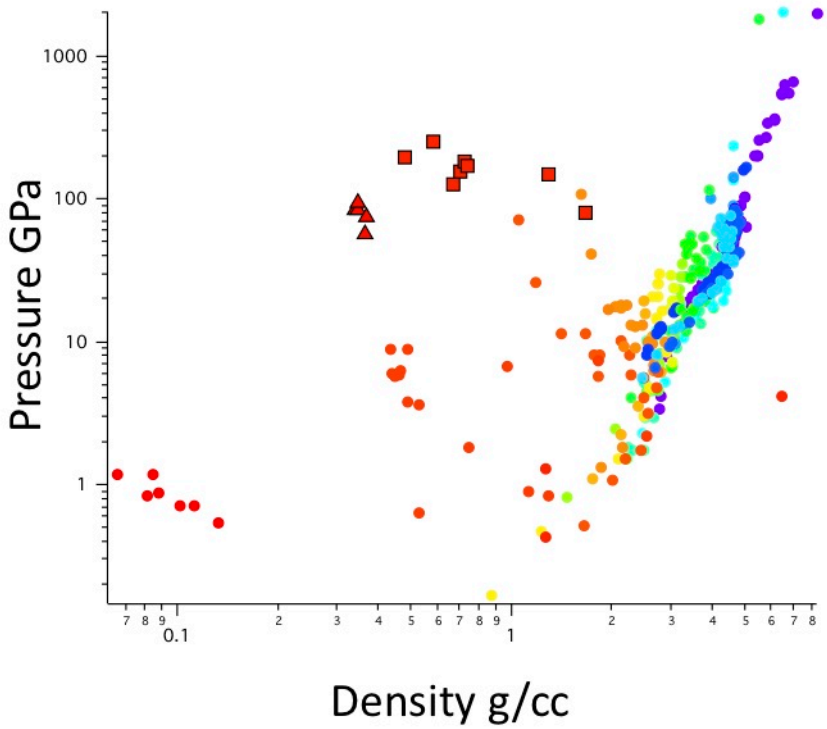

Advanced X-Ray Diffraction Techniques (PI James Hawreliak)

Since the discovery of x-rays by Roentgen over a century ago, x-ray diagnostic techniques have been used for examining the macroscopic structure of samples through radiography, the atomic structure of materials through x-ray diffraction (XRD) and electronic structure of atoms through x-ray spectroscopy. X-ray diffraction has been one of the most widely used techniques for determining a material's atomic structure. It has recently been applied to dynamic experiments, where a shock or ramped pressure wave is applied to a material and then x-rays are flashed in a pump probe experiment to exam the atomic structure as the pressure wave propagates. There is currently an effort to achieve ultrahigh pressure on laser systems using dynamic compression, and in concert with that is the development of new advanced XRD techniques to allow structural probes of the material at high pressure. This campaign was the first implementation of a technique using a Soller slit like array of grids to provide limited line of sight of the detector. Figure 1 shows the effective geometric shielding the Soller slits provide and a sample image of the x-ray source, which is limited to a small portion of the image plate. This is part of an ongoing development project.

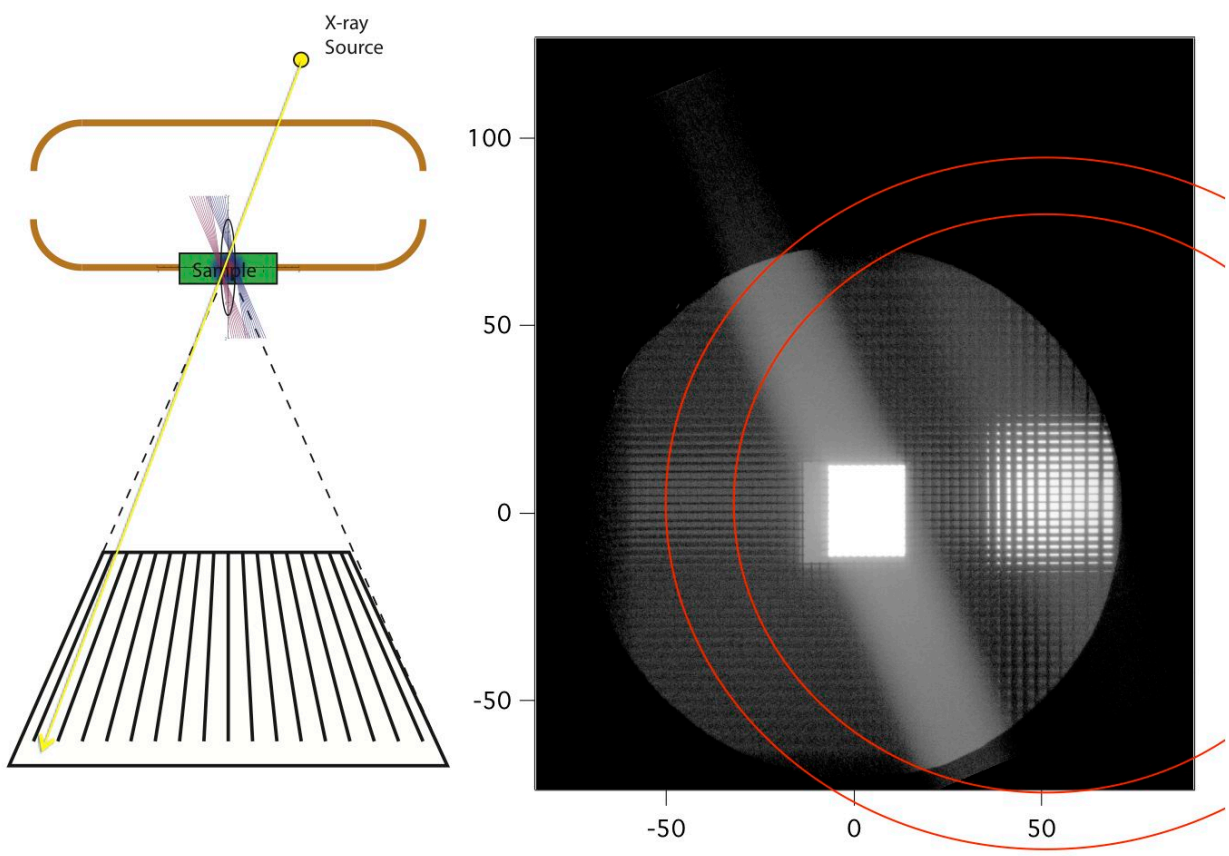

/12/12

II. Radiation Transport

Heated Wall (PI: K. Baker)

The heated wall campaign measured radiation transport in a geometry which enabled the heat wave to propagate as if there were no wall loss. This was accomplished by placing a thin CRF annulus around a low density, 30 mg/cc, SiO2 cylindrical foam. One end of the SiO2 foam and the outer surface of the CRF annulus were heated by the radiation environment inside a hohlraum driven by 15 of the Omega beams. The thickness of the CRF annulus was chosen such that the time dependent position as a function of Z of the supersonic heat wave propagating down the SiO2 cylindrical foam would match the time and Z position of the subsonic heat wave traveling radially inward through the CRF annulus and reaching the SiO2 foam from the side. In this manner the front of the supersonic heat wave traveling along the z-axis of the SiO2 foam did not see a significant radial disparity in radiation temperature and hence propagated as if it were being driven in a 1-D geometry.

The heated wall campaign used the SXI/SSC-A diagnostic to measure the uniformity and breakout time of the supersonic heat wave from the rear of the SiO2 foam. The diagnostic measured breakout times consistent with simulations, including a delayed breakout of the heat wave as the density increased in the SiO2 foam. Two control experiments were performed; one with a gold disk covering the front of the SiO2 foam to block radiation from entering the SiO2 foam along the Z axis and a second replaced the CRF tube with gold to prevent radiation from entering the SiO2 foam from the radial direction. The shot with a cylindrical block showed no evidence of a heat wave reaching the end of the SiO2 foam and the shots with a gold annulus to block radial transport of the hohlraum x rays into the SiO2 foam showed a delayed signal which was significantly weaker and significantly shorter temporal emission as compared to the two heated wall shots.

Crystal Window (PI: B. Maddox)

The CrystalWindow-12A campaign was designed to test fused silica as a VISAR window up to pressures exceeding 50 Mbar (5 TPa). Quartz had been shown to be an excellent high pressure VISAR window at ultra-high pressure. Although quartz blanks at low shock pressure, at higher shock pressure the shockwave in the quartz becomes reflective and can be used to measure the shock velocity transmitting into the quartz crystal. Fused silica is a noncrystalline form of silicon dioxide (SiO_2), the crystalline form being quartz. Due to the amorphous nature of fused silica, it can be polished readily making it an ideal window material for state-of-the-art experiments on the NIF that require non-planar VISAR witness windows. The CrystalWindow-12A campaign used the 15 H7 cones 2 and 3 beams to drive a scale 1 halfraum to 190 eV. The aluminum coated VISAR samples were attached to the open end of the halfraum and were mounted on a 2.65 mm diameter gold washer with a 0.4 mm central aperture to allow collection of the VISAR signal. A 2 mm diameter, 2 mm long gold tube was also mounted on the VISAR side of the target to shield the VISAR optics from any scattered light from the drive laser. Figure 1 shows a picture of the completed target. Two thicknesses of aluminum were tested, 50 um and 70 um, to study any blanking due to pre-heat in the 50 um thick aluminum samples. Additionally, two samples were fitted with reference quartz windows for comparison. Figure 1 also shows VISAR traces for 70 um Al/quartz and 70 um Al/fused silica window targets. The decaying velocity seen here represents the ultra-high pressure shockwave travelling through the quartz and fused silica. The data obtained in this campaign confirmed fused silica works well as a VISAR window at a peak shock pressure of 54.2 Mbar with little to no blanking using a 70 um Al ablator. Some blanking was seen in the 50 um aluminum ablator targets, likely related to x-ray pre-heat.

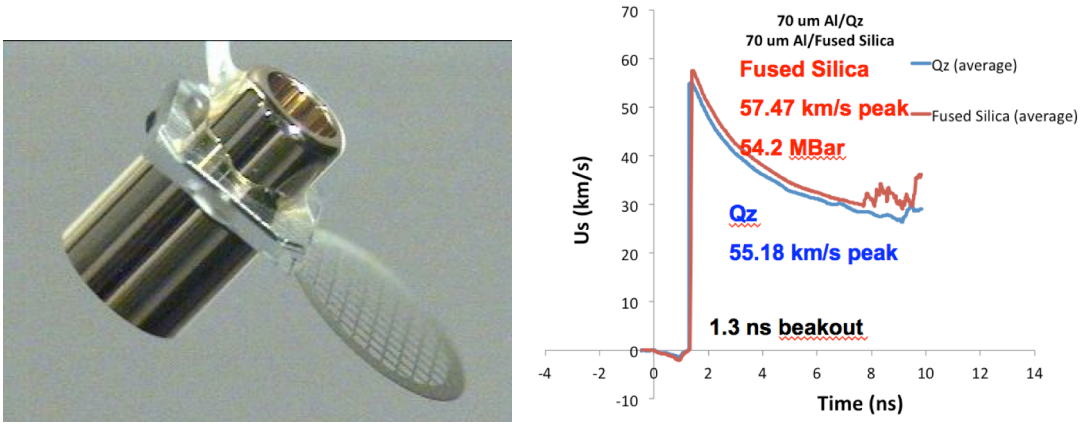

Figure 1. (Left) CrystalWindow-12A target used to verify fused silica as a VISAR window and shock witness material to > 50 Mbar. (Right) VISAR data confirming fused silica working well as a VISAR window at a peak pressure of 54.2 Mbar. The velocity vs. time trace here represents the shockwave travelling through the fused silica and quartz windows.

III. High-Temperature Plasma Opacity

High-Temperature Plasma Opacity Experiments on Omega and Omega-EP (PI: R.F. Heeter with A. Graf, G.V. Brown, C. Mauche and R.E. Marrs)

LLNL's HED opacity research at Omega in FY12 had three main directions. First, the MBOp-12 campaign followed up on physics questions from the very successful 2009-11 Ti opacity shots, where the observed Ti continuum opacity and 1-3 line opacity regions did not match code expectations. New data obtained with a modified hohlraum design indicated up to 50% higher sample temperature was achieved.

The second campaign, NLTE-Dynamics-12, continued previous work on the non-LTE X-ray emission properties of hot high-Z plasmas as found in hohlraums at the laser-driven "hot spots". Uranium was chosen as the sample material due to its use on ignition and other shots on NIF, and due to the paucity of experimental data. Shots performed in FY12 extended earlier work on uranium emission to 2x lower intensity (material temperature) and the data are now being compared with simulations.

The third research direction was the EPOp-12 series, which substantially upgraded the novel short-pulse "absorption-emission" opacity platform developed on Omega-EP in FY10-11. The new platform uses a sample driven with up to 200J via 100 ps FWHM Gaussian UV laser pulses using two of the "long pulse" beams on Omega-EP. The two short-pulse beams deliver up to 1500J in 10 ps to a pair of continuum X-ray backlighters which probe the plasma after some delay. Figure 1 shows the first face-on transmission spectrum obtained from this new platform, using a silicon sample and a probe beam delayed about 300 ps. Multiple L-shell charge states are observed in absorption. Self-emission from helium- and hydrogen-like silicon (produced prior to the backlighter probe but recorded on the time-integrated detector) is also observed. The presence of the Be-like and Li-like ions implies that this new platform achieves temperatures similar to those observed with the single-backlighter platform and titanium samples in FY11.

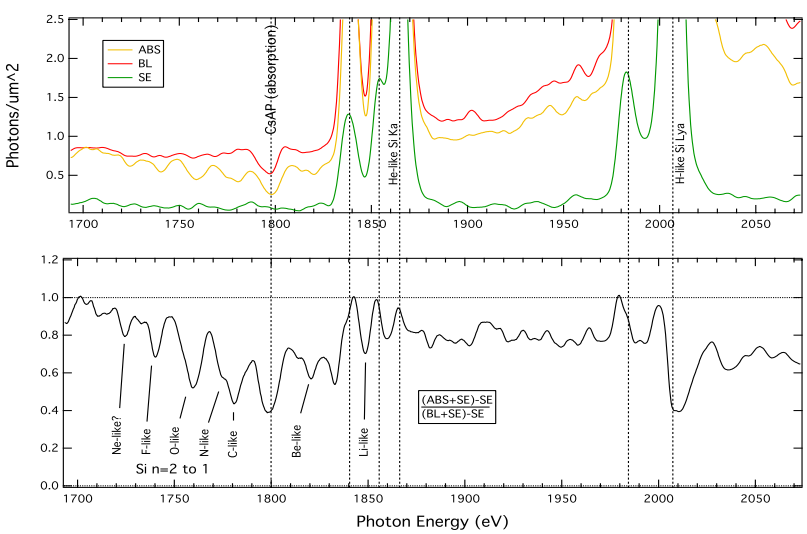

Figure 1: Initial silicon opacity spectra from Omega-EP. Top: Backlighter, sample absorption, and sample self-emission spectra recorded on Biomax film. Bottom: sample transmission.

IV. Burn Physics

Non-LTE Transport, and Nuclear Lifetimes (A. Kritcher)

Plasma coupling to nuclei in high-energy density plasmas, or *nuclear-plasma physics*, is a cutting-edge field that traverses the areas of nuclear physics, plasma physics, and atomic physics. Nuclear-plasma interactions occur in hot and dense plasmas such as inertial confinement fusion environments and astrophysical bodies. The effect of high energy density plasma (HEDP) environments on astrophysical nucleosynthesis, the formation of heavy elements from pre-existing nucleons in astrophysical plasmas, is expected to play a significant role [1]. Nuclei in stellar plasmas reach a thermal population of low-lying excited nuclear states from photo-excitation, free electrons in the plasma (NEEC)[2-5], excitation from atomic transitions (NEET)[6-8], and inelastic electron scattering in the dense plasma. In these experiments we investigate the NEEC process in under-dense plasmas by illuminating mini hot hohlraums (400 or 600 um in diameter) with ~15 kJ of laser light at the Omega laser facility.

The goal of these first experiments was to identify the plasma conditions of hot Tm hohlraums with spectral line emission analysis and optical Thomson scattering, measure the energy and time resolved atomic emission background, investigate this experimental platform to study nuclear lifetime shortening in hot plasmas, and determine the possibility to investigate nuclear-plasma interactions at Omega. In these first experiments we have collected high quality data and are in the process of analyzing the results. Future campaigns will continue to measure plasma conditions of hot hohlraums and investigate nuclear-plasma interactions in HEDP plasma environments. We will also field additional isotopes in this configuration.

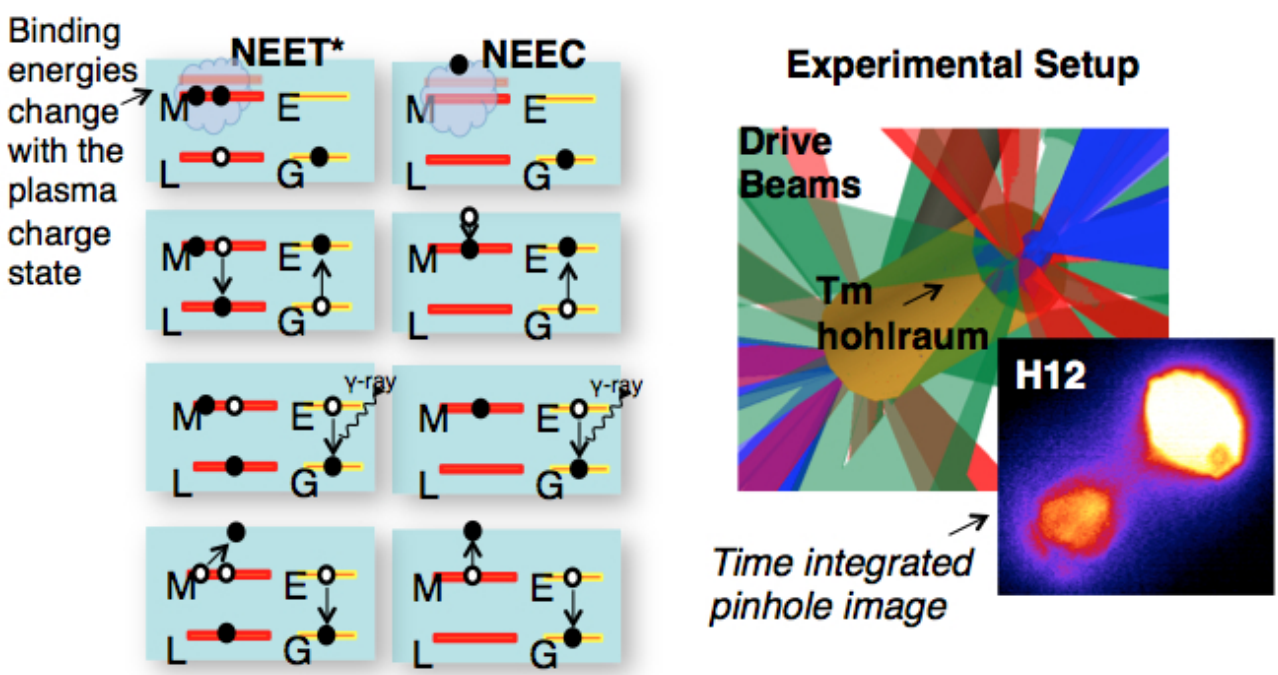

Figure 1: (LHS): Schematic of the NEET and NEEC processes. The red levels on the left hand side denote the atomic shells and the yellow levels on the right hand side denote the nuclear excited and ground states. First, the nucleus in the ground state and atomic shell vacancies are present (and/or free electrons are present). Electrons either transition, or are captured into atomic states and the nucleus becomes excited. The nucleus radioactively decays by gamma-ray emission or internal conversion. (**RHS):** A schematic of the experimental configuration. Tm hohlraums, 400 and 600 um in diameter, are illuminated by near 40 drive beams, a total of 15-20 kJ.

[1] Z. Y. Bao, H. Beer, F. Kappeler, F. Voss, and K. Wisshak, Atomic Data and Nuclear Data Tables 76, 70 (2000).
[2] N. Cue, J. C. Poizat and J. Remillieux, Europhys. Lett., 8, 19-23 (1989).
[3] Adriana Pálffy, et. al., Physics Letters B 661, 330–334 (2008).
[4] Adriana Pálffy, et. al., Physical Rev A 73, 012715 (2006).
[5] M. R. Harston and J. F. Chemin, Physical Rev C, 59, 5, 2462 (1999).
[6] M. Morita and K. Otozai, Hyperfine Interactions 2, 418 (1976).
[7] S. Kishimoto, et. al, Nuclear Physics A 748, 3–11 (2005).
[8] M. R. Harston and J. J. Carroll, Laser Physics, 14, 1452–1456 (2004).

V. Hydrodynamics

Short-pulse, UV backlighting development for NIF (TinMan-12, PI: Vladimir Smalyuk)

High-Energy-Density Complex Hydrodynamics experiments on National Ignition Facility (NIF) require short-pulse backlighting capability. Experiments on OMEGA-EP laser tested short-pulse, UV beam backlighting concept for NIF. Four OMEGA-EP beams were focused onto 10-μm thick Ag wires, mounted on 300 x 300 μm square, 10-μm thick polyimide foils to mimic illumination conditions of one quad on NIF. Total laser energy was ~400 J with ~100 ps Gaussian pulse shape and peak laser intensity of ~$3x10^{16}$ W/cm^2 and a mispointing of <50 μm rms. Three beams were co-timed while the fourth beam was advanced up to 300ps from the co-timed beams to maximize the x-ray backlighter signal. Results were compared with ~1.2 kJ short-pulse (~100 ps) IR beam backlighting with the same Ag-wire targets, driven at intensity of ~$1x10^{17}$ W/cm^2. Figure 1 shows a measured image of the target, created with Ag-wire backlighting on an image plate using HERIE diagnostic located at 50 cm from target chamber center on OMEGA-EP. It consists of the Au grid, used to determine magnification, 100-μm thick Au plate, used to determine resolution, and seven Cu steps with 18 μm thickness between adjacent steps, used to determine contrast and sensitivity. Areas inside and outside of Au plate were also used to measure noise. Figure 2 shows the change in the intensity across the Cu step wedge. The 300 ps advance produced the brightest signal while a 150ps advance produced nominally the same results as all four beams co-timed. The spatial resolution of ~20 μm was similar to IR-beam experiments, while the signal was ~100 times lower. The short-pulse UV backlighting might be feasible for Complex Hydrodynamics experiments on NIF if hohlraum and backlighter x-ray backgrounds do not exceed ~10 PSL on the image plate at 50 cm from NIF target chamber center.

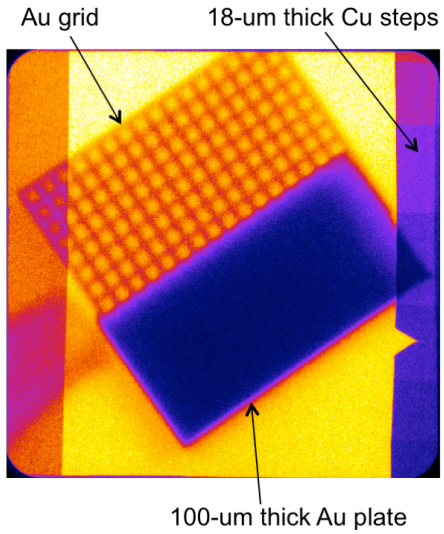

Figure 1. X-ray radiograph of the target consisting of Au grid, 100-μm thick Au plate, and seven 17-μm thick Cu steps.

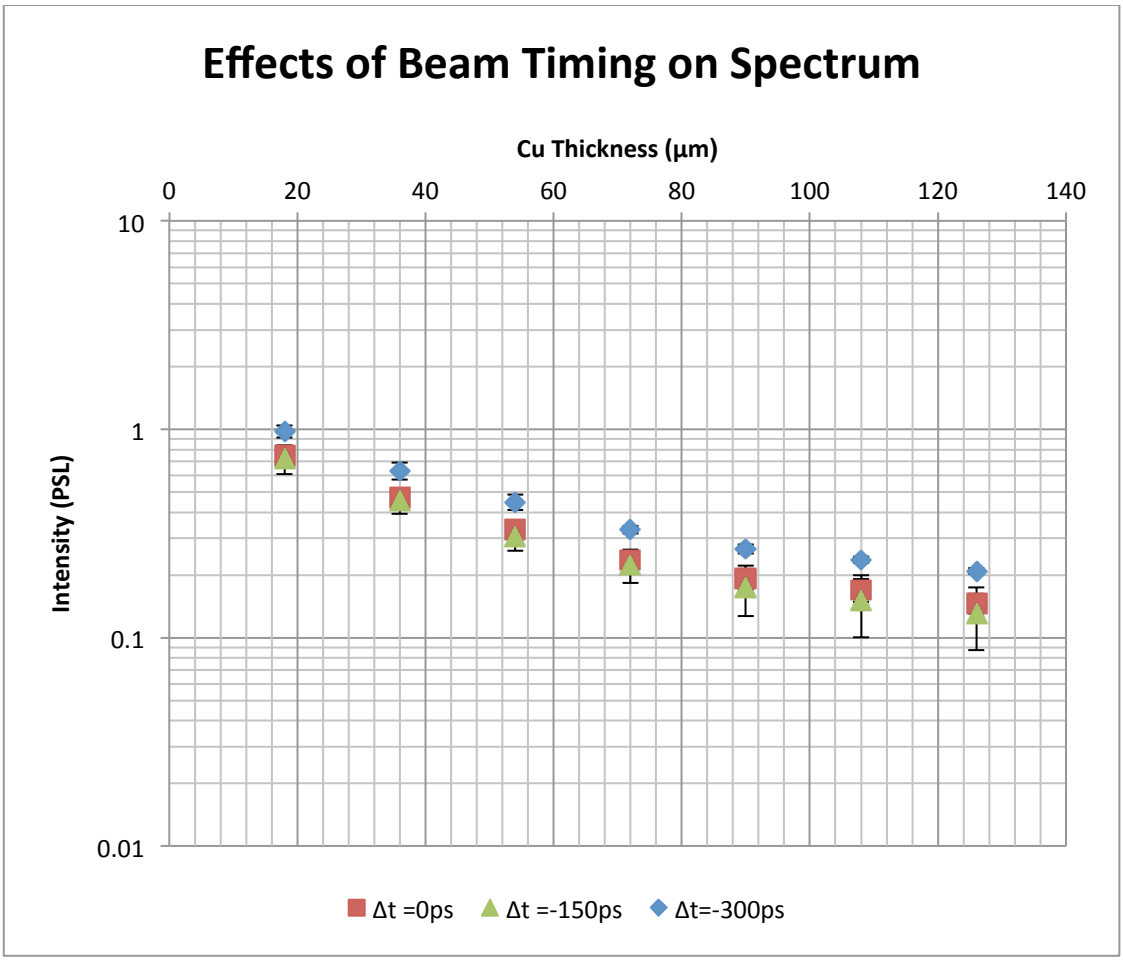

Figure 2. Intensity across the step wedge shows relative differences in backlighter emission. A 300ps advance in beam timing shows a small increase in signal. Uncertainties illustrate shot to shot variation.

VI. X-Ray Source Development and Application

X-ray Source Development with Nanostructured Materials (Nanostructure-12A, PI R. Patterson)

Progress in the fabrication of new metallic aerogels for x-ray generation [F. Pérez et al., Phys. Plasmas **19**, 083101 (2012)] led to a campaign for optimizing titanium x-ray sources, as illustrated in Fig. 1. Experiments were conducted in FY12 by the X-Ray Source Development team in collaboration with the Defense Threat Reduction Agency and researchers from the French CEA. In the FY12 shots, when irradiated by 40 beams of the Omega laser, Ti-doped aerogels (4 mg/cm^3, 4 atomic % of Ti) made by a wet-chemistry process yielded only a 0.7% laser-to-x-ray conversion efficiency in the x-ray band between 4.6 and 5 keV, which is significantly lower than previous record of 3% CE [K.B. Fournier et al., Phys. Rev. Lett **92**, 165005 (2004)]. However, in this campaign novel aerogels were measured to provide a 5.5% CE in the same energy range. These new targets were made by coating SiO_2 aerogel templates with TiO_2. They are of similar ultra-low-density 4 mg/cm^3, but reach a higher Ti concentration (22 at. %).

Current analysis is focused on precise understanding of the x-ray spectra, which will bring interesting new insights to the understanding of the heating of these targets. Analysis will also cover the heating dynamics [C. Constantin et al., Phys. Plasmas **12**, 063104 (2005); M. Tanabe et al., High Energy Density Physics **6**, 89 (2010)] and yield optimization of these targets, using hydrodynamic simulations. The objective is to design future targets by optimizing the Ti concentration and aerogel pore size, which are now controllable.

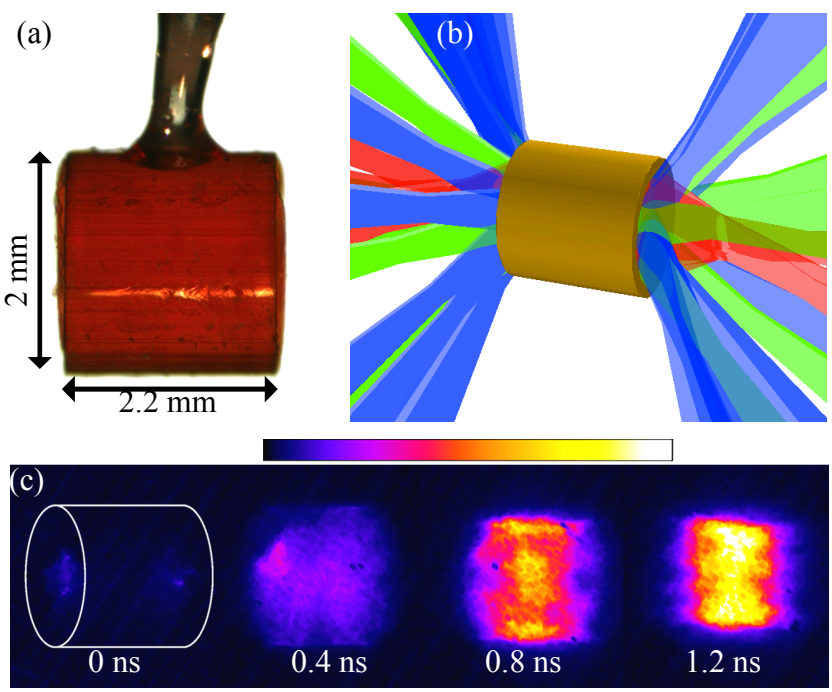

Fig. 12: (a) photograph of a cylindrical aerogel target held inside a thin plastic tube. (b) Irradiation structure from 40 beams of the Omega laser. (c) Example of x-ray emission images at different times relative to the beginning of the interaction.

Solar Cell Electrostatic Discharge (SolarCellESD-12A/B, PI R. Patterson)

During FY12, the X-Ray Source Development team, in collaboration with the Naval Research Laboratory and the Defense Threat Reduction Agency, conducted a series of experiments to examine the effects of x-ray loading on solar cells. Our tests were broken into two parts; we first evaluated the ability of the OMEGA facility to produce a laboratory environment suitable for conducting electrostatic discharge experiments on solar cells, then we subsequently conducted the first tests of active solar cell arrays. For each of these experiments, Fe- or Ge-based targets positioned at the center of the target chamber were irradiated with ~20kJ in a 1 ns square pulse. The XRSA Langmuir Probe Diagnostic (XLPD) or a modification including active solar cells was positioned a few tens of cm from the target.

Building on initial tests in the previous year, we deployed XLPD configured as an array of eight cylindrical Langmuir probes (Fig. 1A) on Feb. 29, 2012 in order to observe the arrival of the source plasma. Time-of-flight measurements resulted in an observed velocity of ~16 ± 2 cm/μs for the leading edge of the source plasma [Patterson et al., Rev. Sci. Instrum. **83**, 10D725 (2012)]. Based on these measurements, we concluded that the OMEGA target chamber is suitable for conducting electrostatic discharge experiments on solar cells, provided that the cells are positioned sufficiently far from the target.

On Sept. 12, 2012, we did indeed place an array of two solar cells along with four standard XLPD probes (Fig. 1B) a minimum of 40 cm from target chamber center to examine the response of these cells to the x-ray and plasma environment produced from Ge-aerogel targets. Fig. 2 shows the prompt x-ray response of the probes as well as the solar cells. In addition, the Langmuir probes show signals consistent with sheath formation in the first two hundred ns, followed by the arrival of charged particles from the target. While our analysis of the solar cell data is ongoing, the data is consistent with an electrostatic discharge; perhaps caused by current flowing to ground through the dense plasma formed from the ablation of the XLPD cassette itself. In future experiments, we will insulate the solar cells from the chassis in order to test the potential arc formation between cells.

Fig. 1: A) shows an XLPD cassette with four pairs of Langmuir probes. Each pair is composed of one 2.5cm and one 20cm probe. B) shows the modification of XLPD to include an active solar cell array. Two 2 x 2 cm Ge triple-junction solar cells are biased up to 100V and can be fielded with up to two pairs of standard XLPD Langmuir probes.

Fig. 2: Initial results from the solar cell discharge experiments. Signals from two ion-collecting probes are shown in addition to the signal recorded from a solar cell biased at 100V.

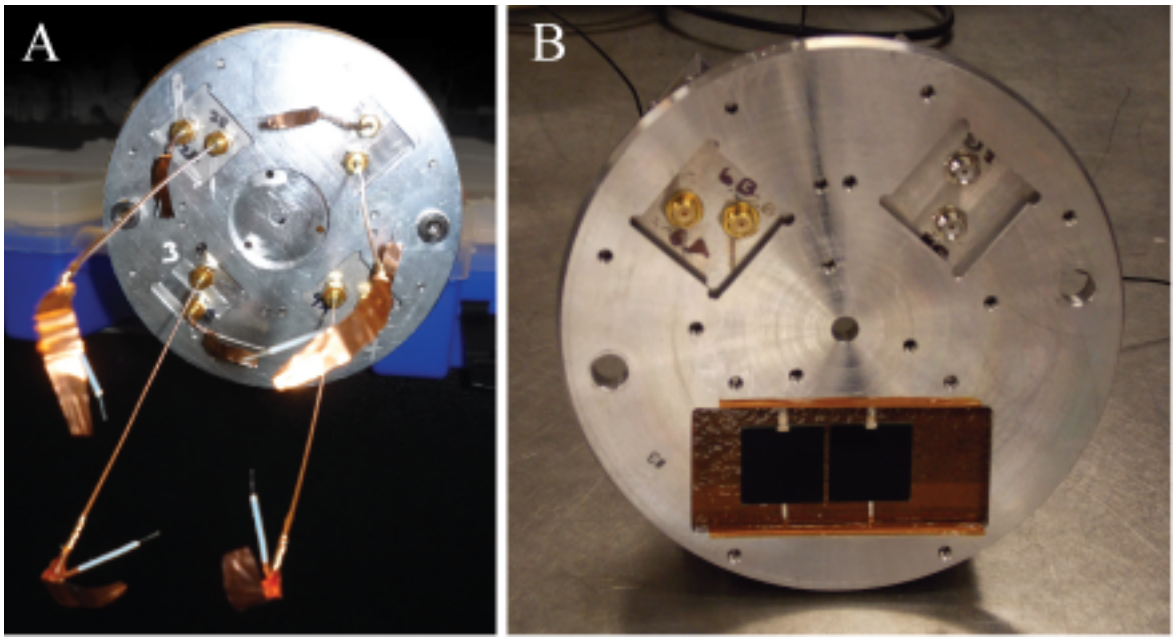
A
B

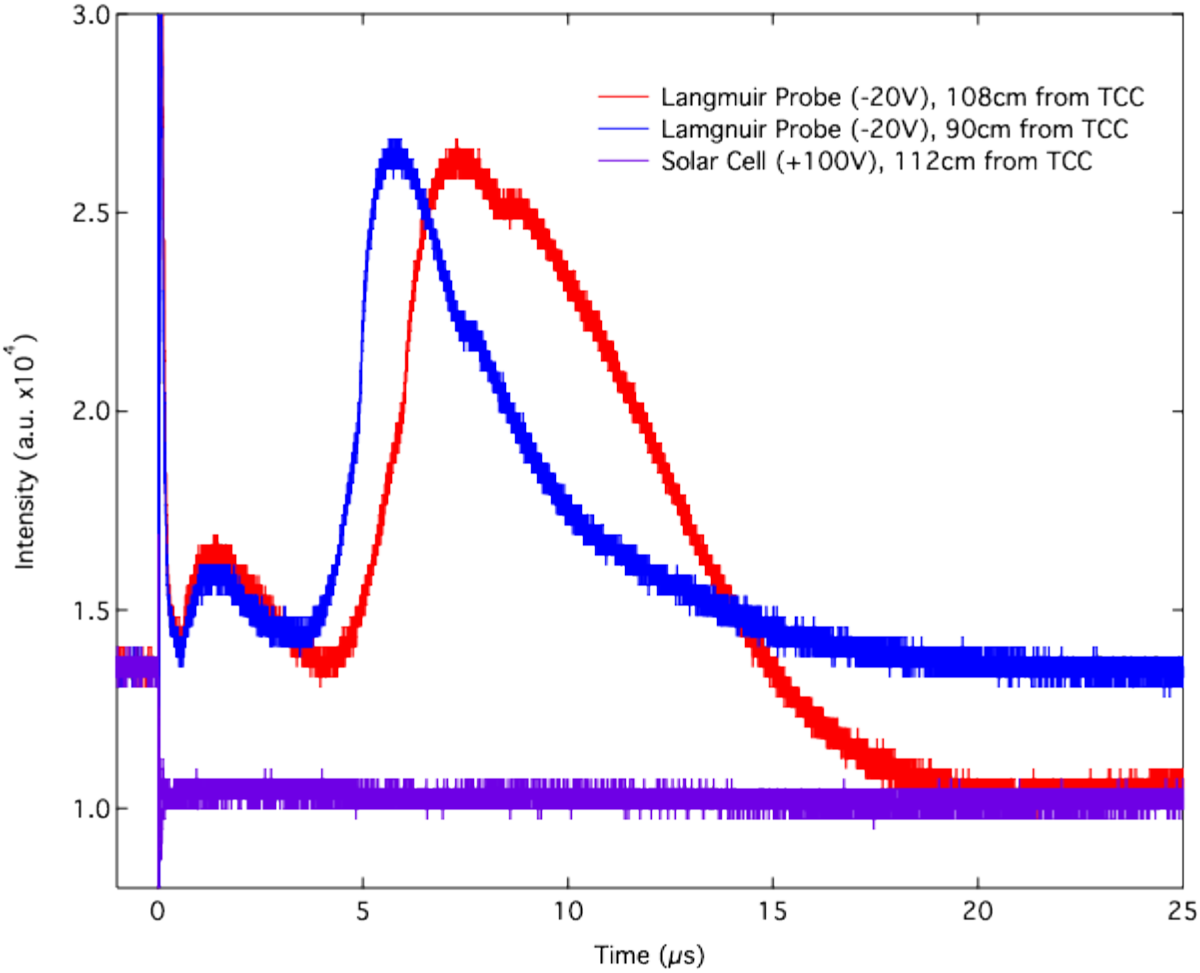
Langmuir Probe (-20V), 108cm from TCC
Lamgnuir Probe (-20V), 90cm from TCC
Solar Cell (+100V), 112cm from TCC
Intensity (a.u. x10^4)
3.0
2.5
2.0
1.5
1.0
0
5
10
15
20
25
Time (μs)